

# Mining Circumgalactic Baryons in the Low-Redshift Universe

Cameron J. Liang<sup>1\*</sup>, Hsiao-Wen Chen<sup>1†</sup>

<sup>1</sup>*Department of Astronomy & Astrophysics, and Kavli Institute for Cosmological Physics, University of Chicago, Chicago IL 60637*

19 October 2018

## ABSTRACT

This paper presents an absorption-line study of the multiphase circumgalactic medium (CGM) based on observations of Ly $\alpha$ , C II, C IV, Si II, Si III, and Si IV absorption transitions in the vicinities of 195 galaxies at redshift  $z < 0.176$ . The galaxy sample is established based on a cross-comparison between public galaxy and QSO survey data and is characterized by a median redshift of  $\langle z \rangle = 0.041$ , a median projected distance of  $\langle d \rangle = 362$  kpc to the sightline of the background QSO, and a median stellar mass of  $\log(M_{\text{star}}/M_{\odot}) = 9.7 \pm 1.1$ . Comparing the absorber features identified in the QSO spectra with known galaxy properties has led to strong constraints for the CGM absorption properties at  $z \lesssim 0.176$ . First, abundant hydrogen gas is observed out to  $d \sim 500$  kpc, well beyond the dark matter halo radius  $R_h$  of individual galaxies, with a mean covering fraction of  $\approx 60\%$ . In contrast, no heavy elements are detected at  $d \gtrsim 0.7 R_h$  from either low-mass dwarfs or high-mass galaxies. The lack of detected heavy elements in low- and high-ionization states suggests that either there exists a chemical enrichment edge at  $d \approx 0.7 R_h$  or gaseous clumps giving rise to the observed absorption lines cannot survive at these large distances. Considering all galaxies at  $d > R_h$  leads to a strict *upper limit* for the covering fraction of heavy elements of  $\approx 3\%$  (at a 95% confidence level) over  $d = (1 - 9) R_h$ . At  $d < R_h$ , differential covering fraction between low- and high-ionization gas is observed, suggesting that the CGM becomes progressively more ionized from  $d < 0.3 R_h$  to larger distances. Comparing CGM absorption observations at low and high redshifts shows that at a fixed-fraction of  $R_h$  the CGM exhibits stronger mean absorption at  $z = 2.2$  than at  $z \sim 0$  and that the distinction is most pronounced in low-ionization species traced by C II and Si II absorption lines. We discuss possible pseudo-evolution of the CGM as a result of misrepresentation of halo radius, and present a brief discussion on the implications of these findings.

**Key words:** galaxies:halos – galaxies: dwarf – quasars: absorption lines – intergalactic medium – survey

## 1 INTRODUCTION

Circumgalactic space is thought to contain a vast amount of baryons (e.g. Spitzer 1956; Fukugita 2004) that are both multiphase and dynamic (e.g. Mo & Miralda-Escudé 1996, Maller & Bullock 2004). In principle, this circumgalactic gas provides the fuel necessary for sustaining star formation in galaxies, while at the same time it is also being replenished with both newly accreted (and presumably chemically pristine) intergalactic gas and chemically enriched materials ei-

ther through gas stripping due to satellite interaction or through starburst driven winds. Therefore, circumgalactic space provides a critical laboratory for studying the baryon cycle that regulates star formation and galaxy growth.

Over the past two decades, absorption spectroscopy of background QSOs have provided an effective tool for probing the otherwise unseen, diffuse gas in halos around distant galaxies. While each QSO provides a one-dimensional mapping through each single halo, observing an ensemble of close galaxy and QSO pairs leads to statistical measurements of mean halo profiles (i.e. absorption strength as a function of projected distance) averaged over the entire galaxy sample. Commonly seen transitions in circumgalactic space include

\* E-mail: jwliang@oddjob.uchicago.edu

† E-mail: hchen@oddjob.uchicago.edu

hydrogen Ly $\alpha$   $\lambda$  1215 (e.g. Lanzetta et al. 1995; Chen et al. 1998, 2001a; Tripp et al. 1998; Wakker & Savage 2009; Steidel et al. 2010; Prochaska et al. 2011; Thom et al. 2012; Stocke et al. 2013; Rudie et al. 2013), the CIV  $\lambda\lambda$  1548, 1550 doublet (e.g. Chen et al. 2001b; Adelberger et al. 2005; Steidel et al. 2010), the MgII  $\lambda\lambda$  2796, 2803 doublet (e.g. Bowen et al. 1995; Chen & Tinker 2008; Kacprzak et al. 2008; Barton & Cooke 2009; Chen et al. 2010a,b; Gauthier et al. 2010; Bordoloi et al. 2011; Werk et al. 2013), and the O VI  $\lambda\lambda$  1031, 1036 doublet (Chen & Mulchaey 2009; Wakker & Savage 2009; Prochaska et al. 2011; Tumlinson et al. 2011; Johnson et al. 2013). A general finding from different studies is that most galaxies are surrounded by chemically enriched gas out to  $\approx 100 - 300$  kpc in projected distance. Competing scenarios for explaining the presence of heavy elements at  $> 50$  kpc from star-forming regions include super galactic winds (e.g. Murray et al. 2011; Booth et al. 2013) and tidally disrupted satellites (e.g. Wang 1993; Gauthier 2013).

A particularly interesting absorption feature to adopt for probing the baryon content of galactic halos is the CIV doublet. These doublet transitions are strong and their rest-frame wavelengths, 1548.20 and 1550.77 Å, enable uniform surveys of chemically enriched gas in the optical window over a broad redshift range from redshift  $z \approx 1$  to  $z \gtrsim 5$ . CIV absorbers are found to originate primarily in photoionized gas of temperature  $T \approx 4 \times 10^4$  K with some contribution from shock heated gas in galaxies and galactic halos (e.g. Rauch et al. 1997; Boksenberg et al. 2003; Simcoe et al. 2004). Therefore, CIV absorption transitions provide an effective tracer of chemically enriched warm gas in and around star-forming regions.

A number of surveys have been carried out to characterize the statistical properties of CIV absorbers found along random QSO sightlines (e.g. Songaila 2001; Boksenberg et al. 2003; Simcoe 2011; Cooksey et al. 2013). While the shape of the CIV equivalent width frequency distribution function appears to remain the same, the total cosmic mass density in C<sup>3+</sup> ions is found to increase from  $z = 4$  to  $z \approx 1.5$  by a factor of 2 (e.g. Cooksey et al. 2013). The increasing CIV mass density together with an increasing background radiation intensity with decreasing redshift (e.g. Haardt & Madau 2012) indicate an increasing chemical enrichment level with time in the gas traced by the CIV absorption transitions (e.g. Oppenheimer & Davé 2008).

At the same time, only three studies have been carried out to characterize extended CIV gaseous halos around galaxies, two at  $z \lesssim 0.5^1$  and one at  $z \approx 2.2$ . A clear understanding has yet to be established. At  $z \approx 0.4$ , Chen et al. (2001b) studied the incidence of CIV absorbing gas at projected distances  $d \lesssim 300$  kpc from a sample of 50 galaxies. These authors reported the presence of a distinct boundary at a *B*-band luminosity-normalized projected distance of  $\hat{d} \equiv d \times (L_B/L_B^*)^{-0.5} \approx 160$  kpc, beyond which no CIV absorbers are detected. The lack of CIV absorption is based on a subsample of 35 galaxies that occur at  $\hat{d} > 160$  kpc from their background QSO sightlines. In contrast, 14 of the 15 galaxies at  $\hat{d} < 160$  kpc have an associated CIV ab-

sorber, although the rest-frame absorption equivalent width,  $W_r(1548)$ , exhibits a large scatter between individual galaxies. At  $z \approx 2.2$ , Steidel et al. (2010) examined the mean spatial absorption profiles of 512 galaxies based on stacked spectra of background galaxies that occur at  $d \lesssim 125$  kpc. These authors found that the mean CIV absorption strength declines rapidly at projected distances of  $\approx 50 - 100$  kpc. Comparing the observations of Chen et al. (2001b) and Steidel et al. (2010) yielded little distinction in the CIV-traced circumgalactic medium (CGM) at low and high redshifts (Chen 2012). Both the luminosity-normalized spatial extent and mean absorption equivalent width of the CGM around galaxies of comparable mass (but with very different on-going star formation rate) have changed little over the redshift interval  $z = 0.4 - 2.2$ , although there exists a large scatter in  $W_r(1548)$  in the low-redshift study. Nevertheless, a lack of variation in the spatial profile of the chemically enriched CGM between two distinct epochs poses a serious challenge to the theoretical models of gas flows around galaxies (e.g. Hummels et al. 2013; Ford et al. 2013a,b).

On the other hand, Borthakur et al. (2013) targeted a sample of 20 galaxies at  $z < 0.2$  and were able to constrain the incidence of CIV absorbing gas for 17 of these galaxies. Of the 17 galaxies studied, eight occur at  $\hat{d} < 160$  kpc and nine at larger distances. These authors detected CIV absorbers for three of the eight galaxies at  $\hat{d} < 160$  kpc and three of the nine galaxies at  $\hat{d} > 160$  kpc in their sample. The finding of a flat rate of CIV incidence with increasing projected distance is intriguing and appears to be in stark contrast to the earlier finding of Chen et al. (2001b). While Borthakur et al. attributed the detected CIV absorbers to starburst activity in the associated galaxies, it is not straightforward to reconcile the discrepant trend found for extended CIV halos between the Chen et al. and Borthakur et al. samples.

To address the discrepant trend found for extended CIV halos around galaxies at low redshifts and to improve the empirical understanding of how the chemically enriched CGM evolves with time, we have searched public archives to find spectroscopically identified galaxies at small projected distance to a UV bright, background QSO for which high-quality echelle/echellette spectra are already available in the *Hubble Space Telescope* (HST) data archive. Our search has yielded the first large sample of  $\sim 300$  close QSO and galaxy pairs that enables a systematic study of extended CIV halos over the projected distance interval of  $d = 0 - 500$  kpc. As described below, this unique sample allows us to place unprecedented limits on the extent of chemical enrichment around low-redshift galaxies based on observations of not only the CIV absorption doublets but also a whole host of ionic transitions from low- and intermediate-ionization states.

Recently, Tumlinson et al. (2013) carried out a large program to use the Cosmic Origins Spectrograph (COS; Green et al. 2012) on board HST to study the CGM at  $d < 150$  kpc of 44  $L_*$  galaxies at  $z = 0.15 - 0.35$ . This program, known as the ‘‘COS-Halos’’ survey, was designed to map the multi-phase CGM using O VI and other metal-line diagnostics (Tumlinson et al. 2011; Werk et al. 2013). The low-redshift cut at  $z = 0.15$  was dictated by the requirement of detecting the O VI doublet using COS and the FUV channel. However, the spectral coverage of the COS FUV grat-

<sup>1</sup> Though we have recently learned that Bordoloi et al. (2014) has also been conducting a survey of CIV absorbers in halos around low-redshift galaxies.

ings misses the CIV doublet at  $z \gtrsim 0.15$ , and therefore CIV transitions are not included in the COS-Halos analysis (e.g. Werk et al. 2013).

Our study differs from the COS-Halos program in two fundamental aspects. First, our search is designed to probe the CIV absorption in galactic halos for comparisons with high-redshift studies. Second, because fainter galaxies are also more numerous, it is more likely to find a faint foreground galaxy near a QSO sightline than a luminous galaxy (see the discussion in § 2). As a result, low-luminosity ( $< 0.1 L_*$ ) and low-mass ( $< 0.1 M_{\text{star}}^*$ ) dwarf galaxies contribute to a large fraction ( $\approx 50\%$ ) of our random QSO and galaxy pair sample. Therefore, *our study complements the COS-Halos effort both in terms of the mass regime of the galaxies and in terms of the ionization state of the CGM.*

Here we report initial findings for the low-redshift CGM based on a sample of 195 galaxies for which constraints on the stellar mass are available. The available stellar mass estimate of each galaxy allows us to infer the total mass of the dark matter in which the galaxy resides (e.g. Behroozi et al. 2013; Kravtsov et al. 2014). This in turn allows us to assess the intrinsic size differences between different galaxies based on the estimated dark matter halo radius from a standard halo model. While the CGM is expected to be regulated by various complicated physical processes, including gravitational motion and star formation feedback, addressing the effects of all these processes at once is challenging. As a first step toward establishing a clear understanding of the processes that drive the observed CGM properties, we have designed our study here to account for the intrinsic size differences (driven by the gravitational potential) of individual galactic halos by normalizing the observed projected distances with the underlying halo radius. We expect that the results will facilitate future studies that consider the effect of additional processes such as star formation feedback.

This paper is organized as follows. In Section 2, we describe the selection criteria for establishing the close galaxy–QSO pair sample and summarize the properties of the galaxy members in the pair sample. In Section 3, we describe the data reduction and analysis procedures of the absorption spectra of the QSOs. In Section 4, we examine the correlation between the strengths of different ionic transitions and galaxy properties, and compare the results of our study with previous findings. Finally, we discuss the implication of our results in Section 5. Throughout the paper, we adopt the standard  $\Lambda$  cosmology,  $\Omega_\Lambda = 0.7$ ,  $\Omega_M = 0.3$  with a Hubble constant  $H_0 = 70 \text{ km s}^{-1} \text{ Mpc}^{-1}$ .

## 2 A PUBLIC SAMPLE OF GALAXY–QSO PAIRS

We have assembled a large sample ( $n_{\text{gal}} \sim 300$ ) of spectroscopically-identified galaxies that occur at small projected distances  $\lesssim 500$  kpc from the sightline of a background UV bright QSO. This galaxy sample is ideal for characterizing extended gaseous halos around galaxies based on the absorption features imprinted in the spectra of the background QSOs.

We first searched the HST archive for QSOs that have been observed with either the Space Telescope Imaging Spectrograph (STIS; Woodgate et al. 1998) or the Cos-

mic Origins Spectrograph (COS; Green et al. 2012) as of Cycle 20. This search yielded a sample of 150 QSOs at  $z_{\text{QSO}} = 0.058 - 1.476$ . Next, we searched for spectroscopically identified galaxies in public archives, including the Nearby General Catalog (NGC; Sinnott 1988), the Sloan Digital Sky Survey (SDSS; York et al. 2000) spectroscopic galaxy sample, the Two Micron All Sky Survey (2MASS) galaxies (Huchra et al. 2012), and the Two Degree Field Galaxy Redshift Survey (2dFGRS; Colless et al. 2001). A galaxy and a background QSO were considered a suitable pair if they satisfied the following criteria. (1) At the redshift of the galaxy, the physical projected distance  $d$  between the galaxy and the QSO sightline is  $d \lesssim 500$  kpc. (2) The galaxy must be at  $|\Delta v| > 10000 \text{ km s}^{-1}$  below the redshift of the QSO to avoid ambiguity between foreground absorbers and those originating in QSO outflows (e.g. Wild et al. 2008). The maximum separation limit of 500 kpc is sufficiently large to encompass the gaseous halos of  $L_*$  galaxies known empirically (e.g. Chen et al. 1998, 2001a; Gauthier et al. 2011; Prochaska et al. 2011; Rudie et al. 2012). It is also motivated by theoretical expectations of extended halo gas out to  $\sim 300$  kpc in radius from star-forming regions (e.g. Ford et al. 2013a). Therefore, including pairs separated by greater than 300 kpc allows us to explore the presence of chemically enriched gas beyond the fiducial virial radius of dark matter halos.

Finally, we formed an “isolated” galaxy and QSO pair sample by considering only galaxies without close neighbors, in order to minimize the ambiguity in associating an absorber with a galaxy. Previous studies have also shown that galaxies in group environments tend to have more extended halo gas than isolated galaxies that results in a larger scatter in the observed spatial distribution of absorption strength with projected distance (Chen et al. 2010a, Bordoloi et al. 2011a, and Gauthier & Chen 2011). In our study, a galaxy was considered an “isolated” one, if no other galaxies have been spectroscopically identified within projected separation of  $d = 500$  kpc and velocity separation of  $|\Delta v| = 500 \text{ km s}^{-1}$  were present. These criteria are driven by the model expectation that an  $L_*$  galaxy at  $z = 0$  has a virial radius of  $\approx 300$  kpc and maximum circular velocity of  $\approx 200 \text{ km s}^{-1}$ . We chosen a more conservative limit to allow for uncertainties in galaxy redshifts.

Our search criteria of suitable galaxy and QSO pairs yielded a final sample of 213 “isolated” galaxies that occur at  $d \lesssim 500$  kpc from the sightline of a background QSO for studies of the low-redshift CGM. Excluding 18 galaxies that are in the COS-Dwarfs program (Bordoloi et al. 2014, in preparation) led to a total of 195 galaxies in our sample. The redshifts of the galaxies range from  $z = 0.002$  to  $z = 0.176$  with a median of  $\langle z \rangle = 0.041$ , and the projected distances of the QSOs range from  $d \approx 32$  kpc to  $d \approx 500$  kpc with a median of  $\langle d \rangle = 362$  kpc. The projected distance versus redshift distribution of the galaxies sample is shown in Figure 1, in which the top and right panels display the histograms in redshift and in projected distance, respectively.

To facilitate a detailed investigation of how the observed CGM absorption properties depend on galaxy properties, we also made use of available measurements of rest-frame UV luminosities and stellar mass from the NASA–Sloan At-

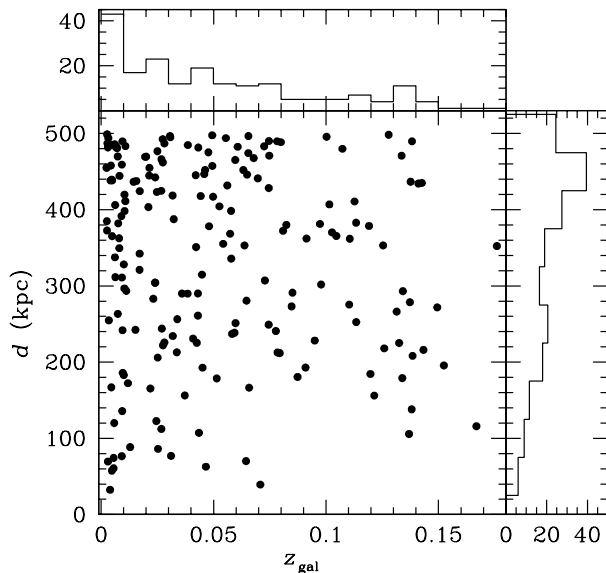


**Figure 1.** Distribution of projected distance versus redshift for the 195 galaxies (§ 2). The top (right) panel displays the redshift (impact parameter) histograms.

las<sup>2</sup> (Blanton et al. 2005; Blanton et al. 2011). This public atlas contains 145,155 galaxies with known redshifts at  $z \lesssim 0.05$ . For each galaxy, it includes optical and UV photometric measurements from the SDSS Data Release 8 (Blanton et al. 2011) and GALEX Data Release 6 (Schiminovich et al. 2007), as well as derived quantities such as stellar mass ( $M_{\text{star}}$ ) and rest-frame UV and optical absolute magnitudes computed by the K-correct code (Blanton & Roweis 2007). The rest-frame UV absolute magnitudes allows us to estimate an unobscured star formation rate (SFR) for each galaxy based on the calibration coefficient of Kennicutt & Evans (2012). The available stellar mass estimate of each galaxy allows us to infer the total mass of the dark matter halo ( $M_h$ ) in which the galaxy resides (e.g. Behroozi et al. 2013; Kravtsov et al. 2014). This in turn allows us to assess the intrinsic size differences between different galaxies based on the estimated dark matter halo radius  $R_h$  from a standard halo model (see § 4 for a more detailed discussion).

Cross-matching the “isolated” galaxy sample with the NASA–Sloan Atlas resulted in 116 overlapping galaxies. We visually inspected the optical images of each galaxy and removed five objects due to erroneous photometry. This exercise resulted in a sample of 111 galaxies with accurate  $M_{\text{star}}$  and star formation rate (SFR) measurements available from the NASA–Sloan Atlas. However, to utilize the full “isolated” galaxy sample for investigating how the observed CGM absorption properties depend on galaxy properties, we needed to estimate the stellar mass for each of the remaining 100 galaxies based on available photometric data. We used the subsample of 111 galaxies as a guide. Comparing the stellar mass provided by the NASA–Sloan Atlas with intrinsic luminosities in different bandpasses revealed a tight correlation between  $M_{\text{star}}$  and rest-frame absolute  $r$ -band magnitude,  $M_{\text{SDSS},r}$ , over four orders of magnitude in  $M_{\text{star}}$

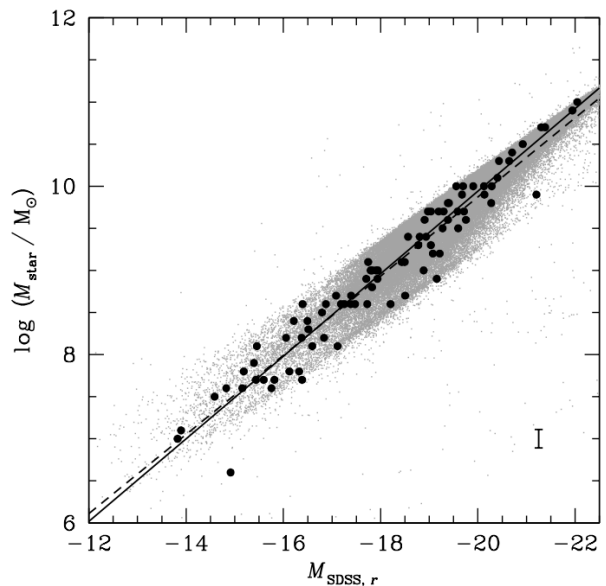


**Figure 2.** Observed correlation between stellar mass  $M_{\text{star}}$  and rest-frame  $r$ -band absolute magnitude,  $M_{\text{SDSS},r}$  for 111 overlapping galaxies that are both in our pair sample and in the NASA–Sloan Atlas (dark solid points). The solid line indicates the best-fit model with  $\log M_{\text{star}} = 0.14 - 0.49 M_r$  and a  $1\text{-}\sigma$  scatter of  $\Delta \log M_{\text{star}} = 0.21$  (error bar in the lower-right corner). The full NASA–Sloan catalog, which has  $> 100k$  galaxies (grey points), is also included to contrast these 111 overlapping galaxies. The full sample displays a consistent mean relation (dashed line) and scatter between  $M_{\text{star}}$  and  $M_r$ . The consistent distribution of the two samples strongly supports that the mean relation derived using the subsample of 111 galaxies is representative of the general galaxy population at low redshifts.

(Figure 2). Based a linear regression analysis, we find that the  $M_{\text{star}}$  vs.  $M_{\text{SDSS},r}$  correlation is best characterized by

$$\log M_{\text{star}} = 0.14 - 0.49 M_{\text{SDSS},r} \quad (1)$$

with a  $1\text{-}\sigma$  scatter of  $\Delta \log M_{\text{star}} = 0.21$ . Equation (1) enables us to obtain a stellar mass estimate and associated uncertainty for galaxies based on  $M_{\text{SDSS},r}$ . In Figure 2, we also include the entire NASA–Sloan catalog, which has  $> 100k$  galaxies (grey points), to contrast the 111 galaxies adopted for deriving Equation (1). The comparison shows that the 111 overlapping galaxies and the full NASA–Sloan catalog share a consistent mean relation and scatter between  $M_{\text{star}}$  and  $M_{\text{SDSS},r}$ , particularly at the high-mass end with  $M_{\text{star}} > 10^{10} M_{\odot}$ . Equation (1) is therefore representative of the general galaxy population at low redshifts.

We present the distribution of stellar masses of our galaxies in Figure 3. The blue shaded histogram shows the stellar mass distribution for the full sample of 195 galaxies, while the black open histogram shows the stellar mass distribution for the subsample of 102 galaxies with  $M_{\text{star}}$  inferred from  $M_r$  following Equation (1). Figure 3 shows that the galaxies in the full sample span a wide range in stellar mass, from  $M_{\text{star}} = 1.5 \times 10^5 M_{\odot}$  to  $M_{\text{star}} = 1.4 \times 10^{11} M_{\odot}$ , with a median  $\langle M_{\text{star}} \rangle = 5.0 \times 10^9 M_{\odot}$ , which is  $\approx 0.1 M_{\text{star}}^*$  (Baldry et al. 2012; Muzzin et al. 2013). Comparing the blue shaded and black open histograms shows that including galaxies with  $M_{\text{star}}$  inferred from Equation (1) allows us

<sup>2</sup> <http://nsatlas.org/>

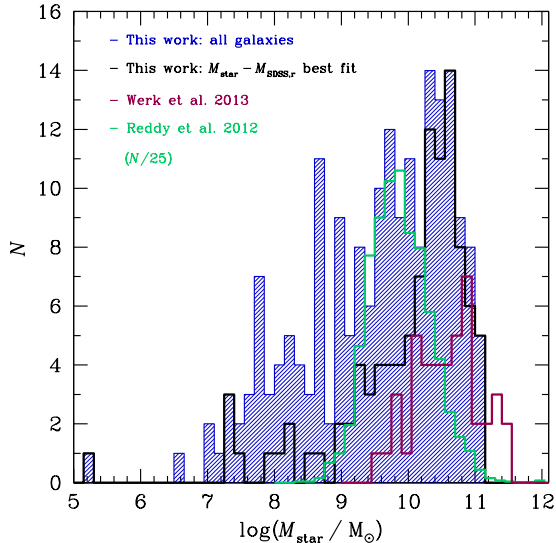


**Figure 3.** Stellar mass distribution of our galaxy sample (blue shaded histogram). The median mass is  $\langle M_{\text{star}} \rangle = 5 \times 10^9 M_{\odot}$ , in comparison to the characteristic mass  $M_{\text{star}}^* = 5 \times 10^{10} M_{\odot}$  for the field galaxies (Baldry et al. 2012; Muzzin et al. 2013). Our galaxy sample has a mass distribution that encompasses previous CGM studies at both low and high redshifts. Specifically, the COS-Halos sample at  $z = 0.1 - 0.4$  (Werk et al. 2013; red open histogram) has a median stellar mass of  $4 \times 10^{10} M_{\odot}$  and the starburst sample at  $z = 2.2$  from Reddy et al. (2012; green open histogram) has a median stellar mass of  $7.9 \times 10^9 M_{\odot}$ . The number counts of the Reddy et al. sample has been reduced by a factor of 25 for presentation purpose.

to expand our CGM study to include higher-mass galaxies, covering a mass range that overlaps with the COS-Halos sample at  $z = 0.1 - 0.4$  (Werk et al. 2013; red open histogram) and the starburst sample at  $z = 2.2$  from Reddy et al. (2012; green open histogram)<sup>3</sup>.

In addition, examining the SFR versus  $M_{\text{star}}$  correlation helps to characterize the galaxies in our pair sample in the context of the general galaxy population. Considering the 111 galaxies with both  $M_{\text{star}}$  and rest-frame UV photometric measurements from the NASA-Sloan Atlas, we present in Figure 4 the specific Star Formation Rate (sSFR; SFR per unit stellar mass) and stellar mass of these galaxies (solid points) in comparison to the mean relations of star-forming main sequence galaxies (blue line) and passive, red galaxies (red) from Schiminovich et al. (2010). Recall that we measured an unobscured SFR for each galaxy based on the observed NUV flux without correcting for possible dust extinction. Therefore, our measurements likely represent lower limits to the intrinsic SFR. The tilt in the distribution of our

<sup>3</sup> We note that while different galaxy samples overlap in the stellar mass range, there are strong distinctions in SFR and in the knowledge of environments and redshift precisions. Specifically, the starburst sample at  $z = 2.2$  has a mean SFR of  $\sim 30 M_{\odot} \text{ yr}^{-1}$  (e.g. Erb et al. 2006) and low-redshift galaxies have on average unobscured SFR of  $\sim 0.1 M_{\odot} \text{ yr}^{-1}$ . In addition, while our sample only includes galaxies in an isolated environment, the environments of the high-redshift starburst sample are unknown.

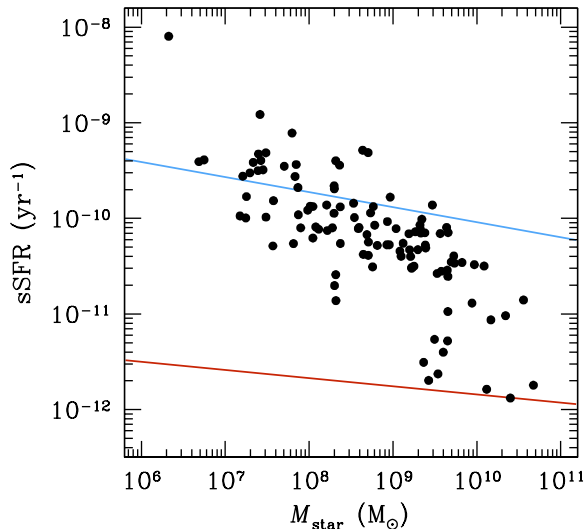


**Figure 4.** Distribution of specific star formation rate (sSFR) and stellar mass based on a subsample of our galaxies with available UV photometric from the NASA-Sloan Atlas (solid points). SFR is derived based on the observed NUV flux from GALEX and therefore represents a lower limit to the intrinsic value. The blue (red) line marks the star-forming main-sequence (passive, red) galaxies from Schiminovich et al. (2010). The tilt in the distribution of our galaxies relative to the mean relation of star-forming main-sequence galaxies can be explained by more massive galaxies showing higher degrees of dust extinction (e.g. Zahid et al. 2013). Nevertheless, the majority of our galaxies are consistent with being star-forming main-sequence galaxies, and a small fraction are found in the red-sequence regime.

galaxies relative to the mean relation of star-forming main-sequence galaxies can be explained by the observed correlation between dust extinction and stellar mass, namely more massive galaxies on average exhibit higher degrees of dust extinction (e.g. Zahid et al. 2013). It is clear that the majority of the galaxies in our sample are consistent with being star-forming main-sequence galaxies with a small fraction found in the red-sequence regime.

We note that while the stellar mass derived using the K-correct code may be systematically overestimated by 0.1 dex in the low mass regime of  $M_{\text{star}} \lesssim 10^{10} M_{\odot}$  (e.g. Moustakas et al. 2013), such error translates to a systematic uncertainty of  $\approx 0.06$  dex in  $M_h$ , well within the scatter in the stellar-mass-to-halo-mass relation of Behroozi et al. (2013). The resulting uncertainty in  $R_h$  is then negligible.

Of the 195 galaxies in our pair sample, 12 occur within 100 kpc in projected distance from a background QSO sightline. We summarize the properties of the galaxy sample in Table 1, which lists for each galaxy the identification, right ascension (RA) and declination (Dec), spectroscopic redshift ( $z_{\text{gal}}$ ), unobscured SFR (when available), stellar mass ( $M_{\text{star}}$ ), halo mass ( $M_h$ ), halo radius ( $R_h$ ), and absolute  $r$ -band magnitude  $M_{\text{SDSS},r}$ .

### 3 QSO UV SPECTROSCOPY

Our galaxy sample contains 195 “isolated” galaxies that occur near the sightlines of 96 independent background QSOs

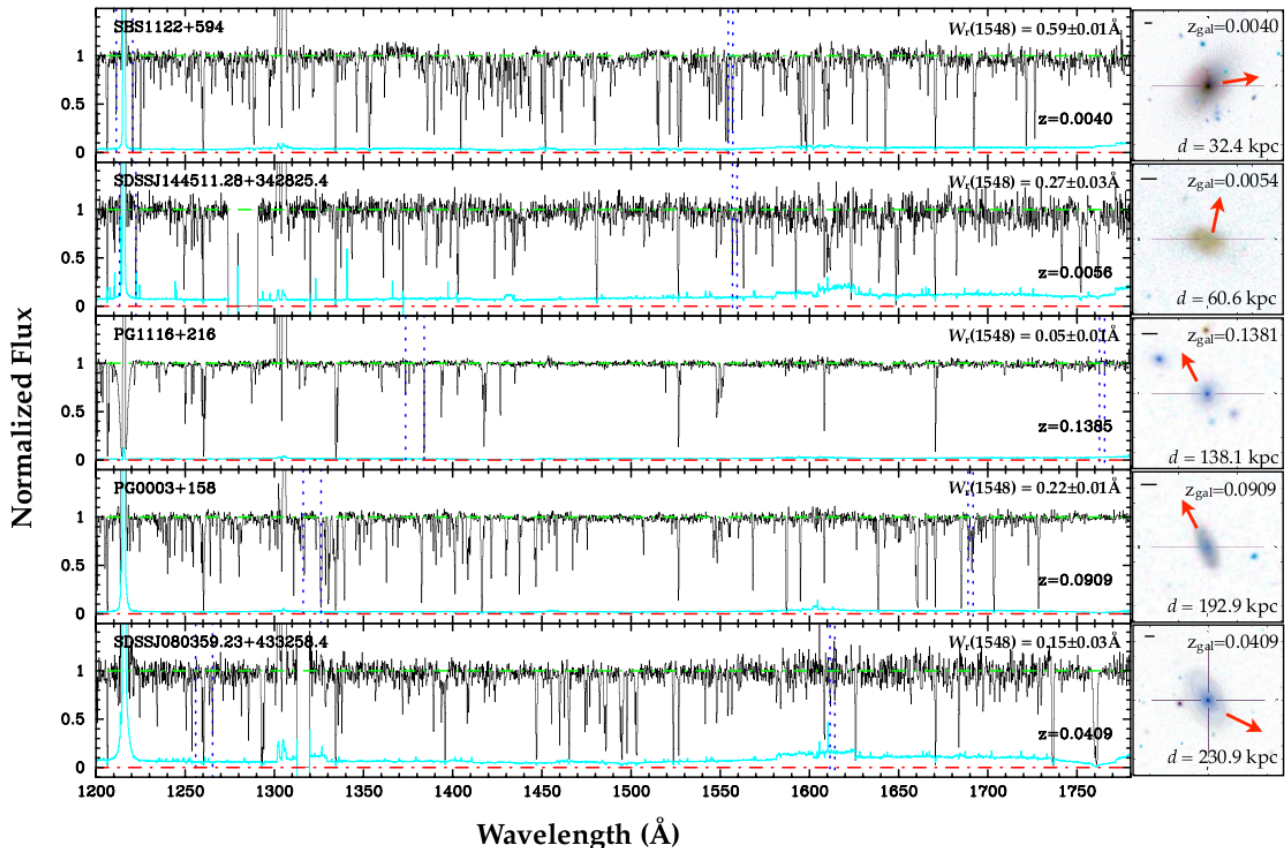


**Figure 5.** Examples of galaxies with associated CIV absorbers from our search. For each field, we present the QSO spectrum in the left panel and the corresponding SDSS image centered at the galaxy in the right panel. In each panel, the direction to the QSO sightline is indicated by the arrow, and the horizontal bar in the upper-left corner indicates an angular scale of  $5''$ . The projected separation between the QSO sightline and the galaxy is shown in the lower-right corner. Absorption features due to Si III  $\lambda$  1206, Ly $\alpha$   $\lambda$  1215, and CIV  $\lambda\lambda$  1548, 1550 at the redshifts of the galaxies are indicated by blue, dotted lines in the left panels. The absorber redshift is shown in the lower right corner of each spectrum.

with high-quality, far-ultraviolet echellette spectra available in the HST data archive. Of the 96 QSOs, 13 were observed using STIS and the E140M grating and 83 were observed using COS and the G130M/G160M gratings. STIS and the E140M grating offers a contiguous spectral coverage from  $\approx 1140 \text{ \AA}$  to  $\approx 1740 \text{ \AA}$  with a full-width-at-half-maximum resolution of  $\text{FWHM} \approx 7 \text{ km s}^{-1}$ , while COS with G130M and G160M at different central wavelengths offers a nearly contiguous spectral coverage from  $\approx 1150 \text{ \AA}$  to  $\lambda \approx 1770 \text{ \AA}$  with a spectral resolution of  $\text{FWHM} \approx 16 \text{ km s}^{-1}$ .

Individual flux-calibrated spectra from STIS were retrieved from the MAST server. For each QSO, individual echelle orders were continuum-normalized and co-added to form a single, stacked spectrum using our own software. The continuum was determined using a low-order polynomial fit to spectral regions that are free of strong absorption features. The mean signal-to-noise ( $S/N$ ) of the combined echelle spectra of 13 QSOs have on average  $S/N > 7$  over the majority of the spectral regions covered by the data.

Individual one-dimensional COS spectra were retrieved from the HST archive and combined using our own software. In summary, individual spectra were first aligned using common absorption lines along each sightline, including both intervening absorbers at  $z > 0$  and known Milky Way

features, such as Si III  $\lambda$  1206 and C II  $\lambda$  1334 in the G130M data and Si II  $\lambda$  1526 and Al II  $\lambda$  1670 in the G160M data. In a few sightlines, the pipeline generated individual spectra exhibit wavelength calibration errors that vary with wavelength, from  $\Delta\lambda \approx -0.06 \text{ \AA}$  at  $\lambda = 1160 \text{ \AA}$  to  $\Delta\lambda \approx +0.06 \text{ \AA}$  at  $\lambda \approx 1600 \text{ \AA}$ . We correct for the wavelength calibration errors by employing a low-order polynomial fit to the observed wavelength-dependent shift in individual spectral segment. Then the individual wavelength-corrected spectra were rebinned to a pixel resolution of  $\delta v = 7.5 \text{ km s}^{-1}$  and coadded into a single combined spectrum using our own co-addition code. The final processed and combined spectra have a median signal-to-noise of  $S/N \approx 2 - 26$ . A summary of the STIS and COS observations for each QSO is presented in Table 2, which lists from columns (1) through (5) the name, RA, Dec, emission redshift of the QSO, and the program ID under which the data were taken. We also list in columns (6) and (7) of Table 2 the median  $S/N$  of the G130M and G160M spectra from COS and in column (8) the median  $S/N$  of the STIS/E140M spectra.

To facilitate absorption-line measurements, we also continuum normalized each QSO spectrum using a continuum model determined from a low-order polynomial fit to spectral regions that were free of strong narrow line features. The

continuum normalization included strong damping wings in each QSO spectrum due to either the Milky Way Ly $\alpha$  absorption or intervening damped Ly $\alpha$  absorbers. We did not attempt to fit strong emission features such as the geocoronal Ly $\alpha$  and O I  $\lambda\lambda$  1302, 1304 lines. These narrow emission lines were instead manually masked and were not included in spectral regions for identifying absorption features.

## 4 ANALYSIS

The process described in § 3 yielded high-quality, continuum-normalized UV echellette spectra of 96 QSOs. These UV spectra allow us to investigate the baryon content of the circumgalactic space within 500 kpc in projected distance of 195 independent, foreground galaxies based on the presence/absence of the corresponding absorption-line features, in particular the CIV doublet. In this section, we describe absorption-line constraints of individual galactic halos. In addition, we present stacked QSO spectra at the rest-frame of the galaxies, and improved absorption-line constraints afforded by the stacked spectra. We show that with much improved  $S/N$ , these stacked spectra allow us to place unprecedented limits for the absorption properties of gaseous halos around galaxies.

### 4.1 Absorption Constraints of Circumgalactic Baryons

In order to obtain robust constraints for the baryon content in halos around our sample galaxies, we first identify and mask contaminating features associated with other strong Ly $\alpha$  absorbers at  $z \leq z_{\text{QSO}}$  along each QSO sightline, including higher-order Lyman series and ionic absorption lines. Then for each of the 195 galaxies, we search in the associated QSO spectra for the corresponding Ly $\alpha$  absorption line within the velocity range of  $|v| \leq 500 \text{ km s}^{-1}$  from the systemic redshifts of the galaxies. The allowed large velocity interval is guided by previous observations (e.g. Lanzetta et al. 1995) which show a velocity dispersion of  $\sim 190 \text{ km s}^{-1}$  between galaxies and their associated Ly $\alpha$  absorbers. For each detected Ly $\alpha$  absorber, we further examine whether associated ionic transitions, such as CIV, CII, SiIV, SIII, and SiII, are also present in the spectral range covered by the STIS/COS data. Absorption transitions considered in our study are summarized in Table 3, together with those considered by Werk et al. (2013) and Steidel et al. (2010) for comparison. We also include in Table 3 the sample size, redshift range, and stellar mass range of each galaxy sample for reference.

We detect associated Ly $\alpha$  absorbers around 125 of the 195 galaxies in our survey sample, and associated CIV absorbing gas in nine galaxies. Roughly 30% of the detected Ly $\alpha$  absorbers show multiple components within a velocity interval of  $500 \text{ km s}^{-1}$  and only one of the nine detected CIV displays an additional secondary component at  $\Delta v = -87 \text{ km s}^{-1}$ . No Ly $\alpha$  (CIV) measurements can be made for 27 (35) galaxies due to the presence of contaminating features. This leaves 43 (151) galaxies that show no trace of Ly $\alpha$  (CIV) absorbing gas at  $d \leq 500 \text{ kpc}$  and  $|v| \leq 500 \text{ km s}^{-1}$ . Examples of the galaxies in our sample that display associated CIV absorbers are presented in Figure 5, which

also highlights the presence of associated SiIII  $\lambda$  1206 and Ly $\alpha$   $\lambda$  1215 in blue dotted lines.

To characterize the absorber properties, we measure the rest-frame absorption equivalent widths for all the observed transitions. We focus our current analysis on absorption equivalent width measurements in order to make direct comparisons with previous studies. A more detailed profile analysis is deferred to a future paper (Liang et al. 2014, in preparation). In cases where an absorption transition is not detected, we measure a  $2\text{-}\sigma$  upper limit to the rest-frame absorption equivalent width over a spectral window that corresponds to the median line width (FWHM) of individual, observed components of the targeted transition from the full sample. For galaxies without associated Ly $\alpha$  absorption, the upper limits of the underlying Ly $\alpha$  and CIV absorption strengths are estimated at the systemic redshifts of the galaxies. For galaxies with associated Ly $\alpha$  absorption but no detectable CIV features, the upper limits of the underlying CIV absorption strengths are estimated at the systemic velocities of the Ly $\alpha$  absorbers which are the velocity centroids of the strongest components determined by the fitting routine described below.

To measure the line widths and velocity centroids of each detected absorber, we model the observed absorption profile as a collection of individual Gaussian components and consider only the minimum number of components necessary to fully describe the observed absorption features. The fitting routine returns for each component the velocity centroid, the  $1\text{-}\sigma$  line width, and the maximum absorption depth. Considering all the individual Ly $\alpha$  components observed in 125 galaxies, we measure a median component line width of  $\text{FWHM}(\text{Ly}\alpha) = 90 \text{ km s}^{-1}$ . Considering all the individual CIV components observed in nine galaxies, we measure a median component line width of  $\text{FWHM}(\text{CIV}) = 49 \text{ km s}^{-1}$ . We note that the observed median line widths are significantly larger than the line width expected of thermal broadening in a warm gas of  $T \sim 4 \times 10^4 \text{ K}$ , which is  $\approx 7.5 \text{ km s}^{-1}$  for CIV absorbing gas. The observed line widths are therefore likely driven by the gas dynamics in galactic halos.

We present in Figure 6 the relative velocity distribution of Ly $\alpha$  and CIV absorbers with respect to the systemic redshifts of the galaxies. Here we also adopt the velocity centroid of the strongest component found in each absorber as the systemic velocity of the absorber. The left panel of Figure 6 shows that the velocity distribution of Ly $\alpha$  absorbing gas around galaxies is best represented by a double Gaussian profile with a narrow component centered at  $\langle v(\text{Ly}\alpha) \rangle = -7 \text{ km s}^{-1}$  and dispersion of  $\sigma_v(\text{Ly}\alpha) = 32 \text{ km s}^{-1}$  and a broad component centered at  $\langle v(\text{Ly}\alpha) \rangle = -8 \text{ km s}^{-1}$  and dispersion of  $\sigma_v(\text{Ly}\alpha) = 188 \text{ km s}^{-1}$  (the solid curve). Excluding the outlier at  $v(\text{CIV}) \approx +260 \text{ km s}^{-1}$ , the velocity distribution of CIV absorbing gas around galaxies can be characterized by a single Gaussian distribution of  $\langle v(\text{CIV}) \rangle = 9 \text{ km s}^{-1}$  and  $\sigma_v(\text{CIV}) = 58 \text{ km s}^{-1}$  (right panel of Figure 6).

However, we note that the sample size of CIV absorbing galaxies is small. It is possible that the difference seen between Ly $\alpha$  and CIV absorbing gas in Figure 6 is driven by sampling uncertainties. To test this possibility, we randomly generated a large number of subsamples of nine Ly $\alpha$  absorbers from the parent sample of 125 Ly $\alpha$  absorbers, and performed a Kolmogorov–Smirnov (KS) test to compare each subsample of Ly $\alpha$  absorbers with the full sample

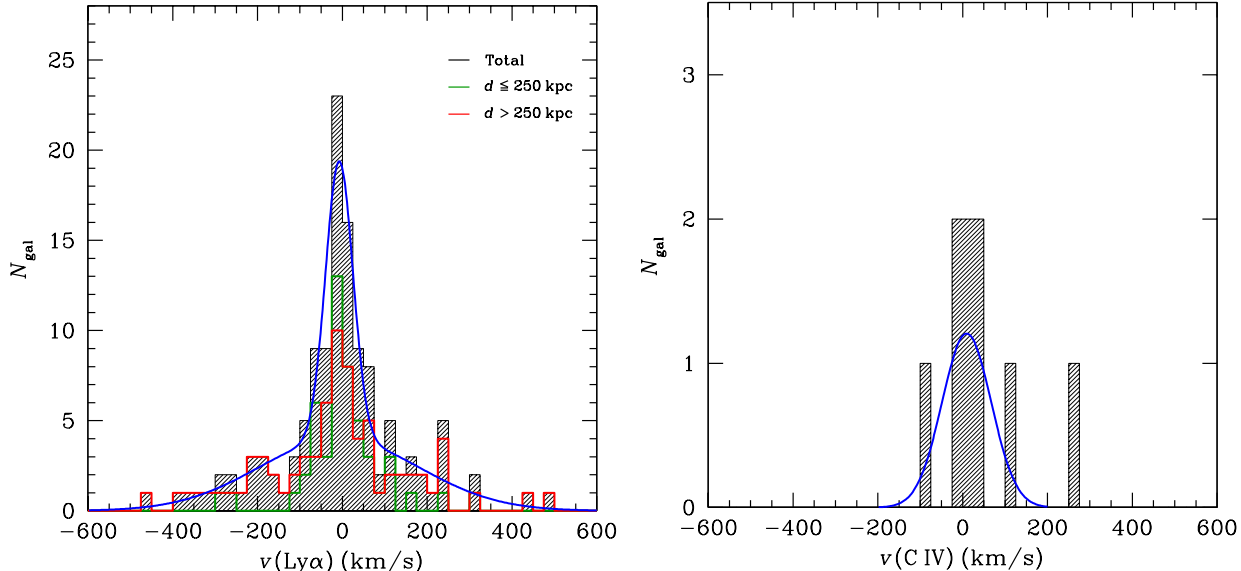


**Figure 6.** Relative velocity distributions of Ly $\alpha$  (*left*) and CIV (*right*) absorbers with respect to the systemic redshift of their associated galaxies in our pair sample. We detect associated Ly $\alpha$  absorbers in 125 of the 195 galaxies searched, and associated CIV absorbing gas in nine galaxies. The left panel shows that the velocity distributions of all Ly $\alpha$  absorbers detected around galaxies at  $d < 500$  kpc (shaded histogram), around galaxies at  $d < 250$  kpc (green open histogram), and galaxies at  $d > 250$  kpc. Considering the full sample requires a double Gaussian profile to characterize the velocity distribution with a narrow component centered at  $\langle v(\text{Ly}\alpha) \rangle = -7$  km s $^{-1}$  and dispersion of  $\sigma_v(\text{Ly}\alpha) = 32$  km s $^{-1}$  and a broad component centered at  $\langle v(\text{Ly}\alpha) \rangle = -8$  km s $^{-1}$  and dispersion of  $\sigma_v(\text{Ly}\alpha) = 188$  km s $^{-1}$  (the solid curve). In contrast, the velocity distribution of CIV absorbing gas around galaxies can be characterized by a single Gaussian distribution of  $\langle v(\text{CIV}) \rangle = 9$  km s $^{-1}$  and  $\sigma_v(\text{CIV}) = 58$  km s $^{-1}$ , excluding the outlier at  $v(\text{CIV}) \approx +260$  km s $^{-1}$ .

of CIV absorbers. Roughly 1/3 of the time, the KS test gives  $> 95\%$  chance that the two samples are drawn from the same underlying parent population. Whether or not Ly $\alpha$  and CIV absorbers share the same origin remains to be tested with a larger sample of CIV absorbing galaxies.

Considering the Ly $\alpha$  distribution alone, we find that that the broad component is dominated by galaxies at  $d > 250$  kpc (red open histogram in the left panel Figure 6). We therefore hypothesize two different origins of the detected Ly $\alpha$  absorbers: (1) halo gas associated with the galaxies contributing primarily to the narrow Gaussian distribution component and (2) intergalactic gas associated with correlated large-scale filaments dominating the broad wings. We suggest that if larger samples of CIV absorbers were found to lack a broad velocity component, that would further support this scenario.

We also repeat the search for C II  $\lambda 1334$ , Si II  $\lambda 1260$ , Si III  $\lambda 1206$ , and Si IV  $\lambda 1393$  absorption features associated with these galaxies. The observed median line width for C II absorbing gas is FWHM  $\approx 67$  km s $^{-1}$ , while the observed median line widths for silicon ions are FWHM  $\approx 27, 36$ , and 47 km s $^{-1}$  for Si II, Si III, and Si IV, respectively. We therefore adopt these velocity intervals for measuring  $2\text{-}\sigma$  upper limits for respective ionic transitions<sup>4</sup>. The observed absorption properties of the gaseous halos around individual

galaxies are summarized in Table 4, which we list for each galaxy the angular separation  $\theta$  from the QSO sightline, the projected proper distance  $d$ , redshift  $z_{\text{gal}}$ , the redshift of the associated Ly $\alpha$  absorber if detected, the measured rest-frame absorption equivalent widths or  $2\text{-}\sigma$  upper limits of different transitions.

## 4.2 Absorption Properties of Individual Galactic Halos

To examine the relation between the incidence and strength of CGM absorption features and galaxy properties, we present in Figure 7 the observed distribution of rest-frame absorption equivalent widths of Ly $\alpha$ , C II, and CIV versus projected distance of the associated galaxy for all galaxies in our galaxy sample. The results can be summarized as follows.

First, robust constraints in Ly $\alpha$  absorption can be determined for 168 galaxies (solid points in the upper-left panel of Figure 7), 43 of which do not have a detectable Ly $\alpha$  absorption feature to a sensitive upper limit (grey, solid points with arrows). All 12 galaxies at  $d < 100$  kpc exhibit a corresponding Ly $\alpha$  absorber, leading to a 100% mean covering fraction of HI absorbing gas within 100 kpc of star-forming regions. Beyond  $d = 100$  kpc, the incidence of Ly $\alpha$  absorption remains high with only 43 of 156 galaxies showing no corresponding Ly $\alpha$  absorption features of  $W_r(1215) \gtrsim 0.1$   $\text{\AA}$ ,

<sup>4</sup> The velocity window adopted here for measuring upper limits of non-detections is empirically determined based on detected components, and is on average 4–6 times smaller than the velocity window adopted by Werk et al. (2013) for determining their

leading to a mean gas covering fraction of  $> 70\%$  over the projected distance interval of  $100 - 500$  kpc from galaxies. In addition, the observed mean Ly $\alpha$  absorption strength gradually declines with increasing  $d$ , consistent with the mean relation reported by Chen et al. (1998, 2001a; solid line). For comparisons, we include measurements and upper limits for  $\sim L_*$  galaxies at  $z = 0.14 - 0.36$  from the COS-Halos program (Werk et al. 2013; open squares) and for starburst galaxies at  $z = 2.2$  from Steidel et al. (2010; green stars).

Second, robust constraints in C II absorption can be determined for 141 galaxies (solid points in the middle-left panel of Figure 7), 134 of which do not have a detectable C II absorption feature to a sensitive upper limit (grey, solid points with arrows). Three of the four galaxies at  $d \lesssim 60$  kpc exhibit associated C II absorption and none of the eight galaxies at  $d = 60 - 100$  kpc show a corresponding C II absorber of  $W_r(1334) > 0.04 \text{ \AA}$ . This leads to a mean covering fraction of  $\approx 67\%$  in C II absorbing gas at  $d \lesssim 60$  kpc of star-forming regions and  $25\%$  at  $d < 100$  kpc. Beyond  $d = 100$  kpc, we detect C II absorption near four additional galaxies at  $d = 106, 116, 138,$  and  $225$  kpc, and the remaining galaxies do not show associated C II absorber to  $2\text{-}\sigma$  upper limits of better than  $W_r(1334) > 0.1 \text{ \AA}$ . The lack of observed C II absorption leads to a strong constraint on the mean C II absorbing-gas covering fraction of  $\approx 3\%$  over the projected distance interval of  $100 - 500$  kpc from galaxies. Likewise, we include measurements and upper limits for  $\sim L_*$  galaxies at  $z = 0.14 - 0.36$  from the COS-Halos program (Werk et al. 2013; open squares) and for starburst galaxies at  $z = 2.2$  from Steidel et al. (2010; star symbols) for comparisons.

A possible explanation for a substantially lower incidence of C II absorption at  $d > 100$  kpc is an increased ionizing radiation field that offsets a larger fraction of carbon atoms into higher ionization states. We examine the incidence of C IV absorption features in the bottom-left panel of Figure 7, where we show that robust constraints in C IV absorption can be determined for 160 galaxies (solid points) and 151 of these do not have a detectable C IV absorption feature to a sensitive upper limit (grey, solid points with arrows). Of the 12 galaxies at  $d < 100$  kpc, four show a corresponding C IV absorber, leading to a mean covering fraction of  $\approx 33\%$  in C IV absorbing gas within 100 kpc of star-forming regions. Beyond  $d = 100$  kpc, five galaxies show associated C IV absorption and the rest do not show corresponding C IV absorption of  $W_r(1548) \gtrsim 0.1 \text{ \AA}$ , leading to a mean C IV absorbing-gas covering fraction of  $\approx 3.4\%$  over the projected distance interval of  $100 - 500$  kpc from galaxies. For comparisons, we include measurements and upper limits for  $\sim L_*$  galaxies at  $z \approx 0.4$  from (Chen et al. 2001b; open triangles) and for starburst galaxies at  $z = 2.2$  from Steidel et al. (2010; pluses). Note that the C IV doublets were not resolved in the stacked spectra of Steidel et al. (2010). We therefore display a possible range of  $W_r(1548)$  based on two extremes in the assumed line ratio (e.g. 2:1 or 1:1) between the C IV  $\lambda 1548$  and C IV  $\lambda 1550$  members.

The QSO spectra also allow us to examine the spatial distribution of silicon ions in the CGM. Figure 8 displays the observed absorption strength of Si II  $\lambda 1260$ , Si III  $\lambda 1206$ , and Si IV  $\lambda 1393$  versus projected distance of the associated galaxy for all galaxies in our sample. We find that the Si II  $\lambda 1260$  transition appears to be contaminated for 37 galaxies, and that only three of the remaining 158 galax-

ies shows associated Si II absorption at  $d = 39, 115,$  and  $138$  kpc. (upper-left panel of Figure 8). With the exception of one galaxy at  $d = 497$  kpc, for which no sensitive limit can be placed due to the poor quality of the data, none of the other 154 galaxies show associated Si II absorption to sensitive limits better than  $0.06 \text{ \AA}$ . In addition, the Si III  $\lambda 1206$  transition appears to be contaminated for 62 galaxies, and eight of the remaining 135 galaxies show associated Si III absorption. Of the 10 galaxies at  $d < 100$  kpc for which constraints for Si III absorption can be obtained, four exhibit associated Si III absorption, leading to a mean Si III covering fraction of  $\approx 40\%$  (middle-left panel of Figure 8). At  $d > 100$  kpc, four of the 125 galaxies exhibit associated Si III, leading to a mean covering fraction of  $\approx 3\%$ . Finally, robust constraints in the Si IV  $\lambda 1393$  absorption can be determined for 150 galaxies, seven of these exhibit associated Si IV absorption with four of the detections found at  $d > 100$  kpc (bottom-left panel of Figure 8). None of the other 143 galaxies show associated Si IV absorption to sensitive limits better than  $0.07 \text{ \AA}$ .

The left panels of Figures 7 & 8 display a stark contrast between the spatial distributions of hydrogen atoms and heavy elements. While hydrogen gas is observed all the way out to 500 kpc in projected distance, the same galaxies that display moderately strong H I absorption do not exhibit associated heavy elements at  $d > 200$  kpc. The lack of heavy elements at large distances persists through all ionization states examined in our study, from low-ionization species such as C<sup>+</sup> and Si<sup>+</sup> ions to high-ionization species such as C<sup>3+</sup> and Si<sup>3+</sup> ions. It indicates that if heavy ions are present in the outer halos, then they remain in a tenuous, hot phase in which gaseous clumps giving rise to the observed absorption lines cannot survive. Similar to Figure 7, we include previous measurements and upper limits for  $\sim L_*$  galaxies at  $z = 0.14 - 0.36$  from the COS-Halos program (Werk et al. 2013; open squares) and for starburst galaxies at  $z = 2.2$  from Steidel et al. (2010; star symbols) for comparisons.

### 4.3 Mass Scaling Of Extended Gaseous Halos

In addition to the distinct spatial extent between hydrogen gas and heavy ions, the left panels of Figure 7 & 8 also display significant scatter in the  $W_r$  versus  $d$  space. In particular, different galaxy samples appear to segregate in different parts of the  $W_r$ - $d$  parameter space. Both the  $z = 2.2$  starburst galaxy sample and the COS-Halos sample contain primarily galaxies at  $d < 100$  kpc, which exhibit on average stronger absorption in Ly $\alpha$  and in ionic transitions. Such distinction appears particularly strong in C II and Si II absorption strengths.

Recall that our galaxies span a broad range of stellar mass with 50% of the sample characterized as low-mass dwarf galaxies of  $M_{\text{star}} < 0.2 M_{\text{star}}^*$ , while the COS-Halos galaxies are primarily  $M_{\text{star}}^*$  galaxies (Werk et al. 2013) and the  $z = 2.2$  starburst sample from Steidel et al. (2010) has a median stellar mass that lies between the COS-Halos and our samples (e.g. Reddy et al. 2012; see also Figure 3). It has been shown empirically at low redshifts that more massive galaxies on average possess more extended gaseous halos (e.g. Chen et al. 2010b). This is also expected by theoretical models (e.g. Mo & Miralda-Escudé 1996; Maller & Bullock 2004; Ford et al. 2013b). As a first step toward establish-

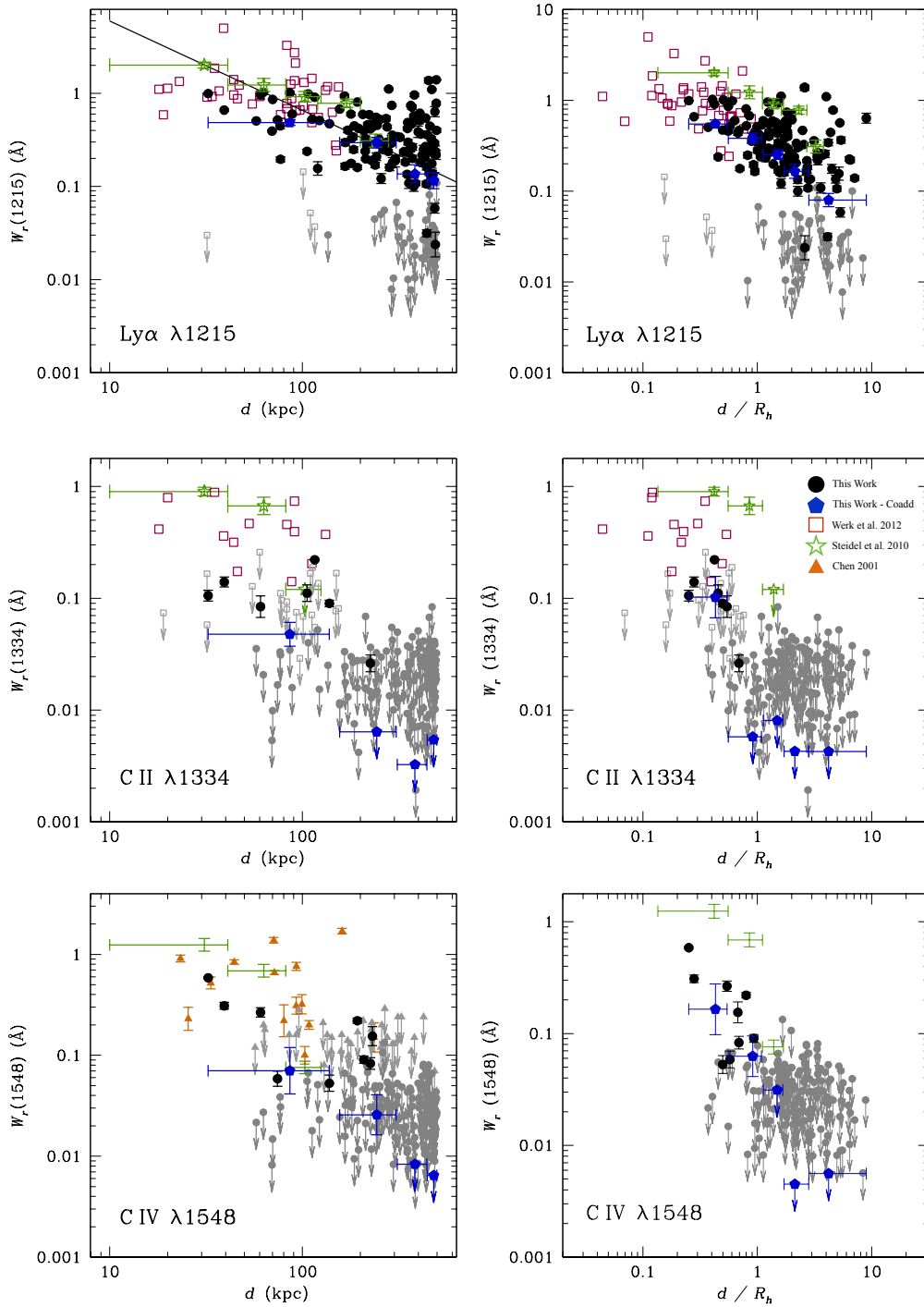


**Figure 7.** Observed spatial distribution of rest-frame absorption equivalent widths of Ly $\alpha$  (top), C II (middle), and C IV (bottom) in the circumgalactic space. The left panels show the variation of absorber strengths versus projected distance  $d$ , while the right panels show the spatial variation as a function of halo-radius ( $R_h$ ) normalized projected distance,  $d/R_h$ . Galaxies with no detectable absorption are shown as  $2\text{-}\sigma$  upper limits (points with downward arrows) that are determined based on the noise characteristics (see § 4.1). Measurements from our study are shown in solid points. Measurements for  $\sim L_*$  galaxies at  $z = 0.14 - 0.36$  from the COS-Halos program (Werk et al. 2013) are shown in open squares. For starburst galaxies at  $z = 2.2$  (Steidel et al. 2010), constraints on Ly $\alpha$  and C II absorption are shown in star symbols. But because C IV doublets were not resolved in this study, a range of  $W_r(1548)$  is shown in vertical bars based on assumed doublet ratios of 2:1 and 1:1. The measurements at  $z = 2.2$  are from stacked spectra of galaxies covering a range in stellar mass (Reddy et al. 2012). Previous measurements of C IV absorption in the low-redshift CGM from Chen et al. (2001b) are shown in triangles. The best-fit power-law model of Chen et al. (1998, 2001a) to describe the observed  $W_r(1215)$  versus  $d$  anti-correlation is shown in solid line. Finally, mean absorption strengths determined from stacked CGM spectra of the full sample (§ 4.4) are shown in (blue) pentagons with the horizontal bars indicating the bin size.

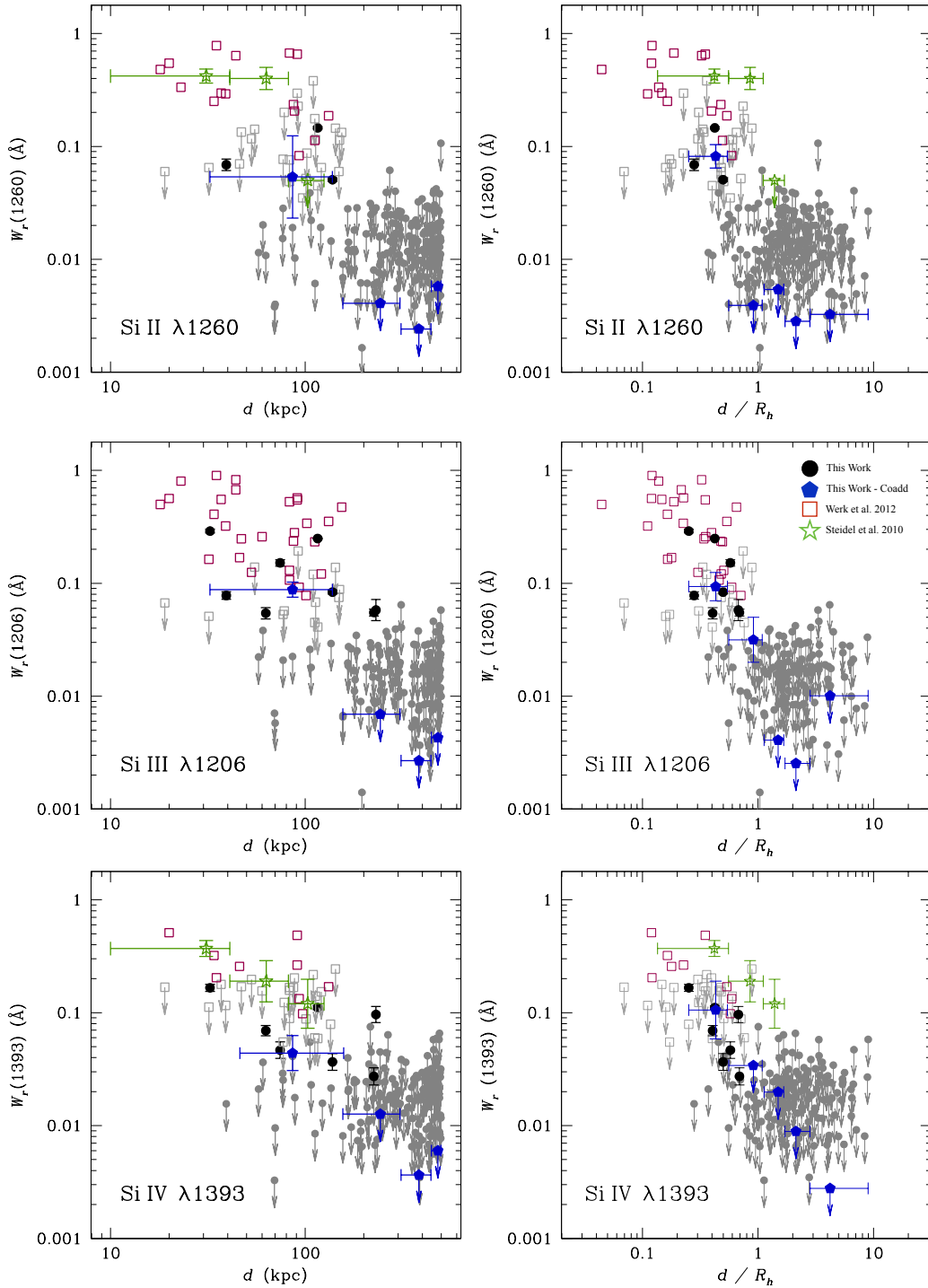


**Figure 8.** Similar to Figure 6 but for the observed spatial distribution of rest-frame absorption equivalent widths of Si II (top), Si III (middle), and Si IV (bottom) in the circumgalactic space. Note that the constraints for non-detections in the COS-Halos sample appear to be worse than our typical upper limits, because the COS-Halos team adopted a much larger velocity window for measuring their upper limits (i.e.  $\approx 300 \text{ km s}^{-1}$  adopted for the COS-Halos galaxies versus  $\approx 50 \text{ km s}^{-1}$  adopted in our study). The velocity window adopted in our study is empirically determined based on detected components, and is therefore more appropriate for constraining the presence/absence of cool, photo-ionized clouds in the circumgalactic space.

ing a clear understanding of the processes that drive the observed CGM properties, it is therefore necessary to investigate whether the apparent distinction in the observed gaseous extent of different galaxy samples can be explained by the intrinsic size differences of individual galactic halos. The results will facilitate future studies that consider the effect of additional processes such as star formation feedback.

To address the possible mass-scaling of gaseous radius, we first estimate the dark matter halo mass  $M_h$  for each galaxy based on its known stellar mass  $M_{\text{star}}$  from the NASA-Sloan Atlas and the stellar mass-halo mass relation of Kravtsov et al. (2014) at  $z \lesssim 0.1$ . We then compute the halo radius  $R_h$ , following the prescription of Bryan & Norman (1998)

$$M_h = \frac{4\pi}{3} \Delta_h \langle \rho_m \rangle(z) R_h^3, \quad (2)$$

where  $\langle \rho_m \rangle(z)$  is the mean matter density of the Universe at  $z$ ,  $\Delta_h$  represents the overdensity over which a halo is defined, and  $\Delta_h = 18\pi^2 + 82x - 39x^2$  with  $x \equiv \Omega_M (1+z)^3 [H_0/H(z)]^2 - 1$ . The halo radius is then computed according to

$$R_h = \frac{261.3}{(1+z)} \left( \frac{\Delta_h(z)\Omega_M}{97.2} \right)^{-1/3} \left( \frac{M_h}{10^{12} M_\odot} \right)^{1/3} \text{ kpc}. \quad (3)$$

Lastly, we divide the projected distance of each galaxy by its halo radius and examine how the observed absorption strengths of different transitions vary with  $R_h$ -normalized projected distance,  $d/R_h$ . The results are shown in the right panels of Figures 7 & 8.

For comparison, we also calculate the halo radius for each COS-Halos galaxy using the published  $M_{\text{star}}$  from Werk et al. (2013), normalize the galaxy projected distance by the corresponding  $R_h$ , and include their absorption measurements in the  $R_h$ -normalized panels. In addition, we adopt the median halo mass of  $\langle \log(M_{\text{star}}/M_\odot) \rangle = 9.9 \pm 0.5$  for the starburst galaxies at  $z = 2.2$  from Reddy et al. (2012). Using a stellar mass-halo mass relation appropriate for high-redshift galaxies from Behroozi et al. (2013), we estimate a mean halo mass of  $\log(M_h/M_\odot) = 11.6 \pm 0.2$  and a mean halo radius of  $R_h \approx 74 \pm 13 \text{ kpc}^5$ . Because the dispersion in  $R_h$  as a result of dispersion in  $M_{\text{star}}$  of the starburst sample is much less than the bin size adopted for  $d$ , we normalize their mean projected distance by a single mean halo radius and include their measurements in the right panels of Figures 7 & 8. We cannot include the earlier CIV measurements of Chen et al. (2001b) because the mass of each galaxy is unknown.

After accounting for a possible mass scaling of gaseous radius, we note three important features in the right panels of Figures 7 & 8. First, the QSOs in our pair sample probe regions as close as  $0.2 R_h$  in galactic halos to  $\approx 10 R_h$  outside of galactic halos. While Ly $\alpha$  absorbers are frequently observed at projected distances much beyond  $R_h$ , no ionic transitions are found at these large radii. The few detections at  $d > 100 \text{ kpc}$  turn out to be associated with most massive

galaxies in the sample and the QSO sightlines appear to still probe the inner halos of these galaxies. The large sample allows us for the first time to place stringent limits on the possible presence of heavy elements beyond galactic halos. We place a strict *upper limit* of 3% (at a 95% confidence level) on the incidence of  $W_\tau > 0.05 \text{ \AA}$  metal-line absorbers over the range of projected distances from  $R_h$  to  $9 R_h$  (see § 4.5 and Figure 11 below).

Second, the COS-Halos sample probes the metal-enriched CGM over the projected distance range from  $\approx 0.05 R_h$  to  $\approx 0.5 R_h$ . Recall that the median mass of the COS-Halos sample at  $z = 0.1 - 0.4$  is  $4 \times 10^{10} M_\odot$  (Werk et al. 2013), while our galaxy sample spans a broad range in stellar mass with a median  $\langle M_{\text{star}} \rangle = 5 \times 10^9 M_\odot$ . Therefore, the COS-Halos sample probes primarily the inner halos of massive galaxies and our galaxy sample extends to outer halos of lower- and high-mass galaxies. The observed absorption strengths versus  $R_h$ -normalized projected distance from the COS-Halos observations now connect smoothly with the measurements for our sample. These include HI, CII, SiII, SiIII, and SiIV. The on average stronger absorbers found around COS-Halos galaxies can therefore be explained by higher gas density in the inner halos, at least around massive galaxies. Considering our sample with the COS-Halos sample together shows that both the absorption strengths and incidence (covering fraction) of heavy elements decline steeply beyond  $0.3 R_h$  and no heavy ions are detected beyond  $\approx 0.7 R_h$ .

Finally, the starburst galaxy sample probes the metal-enriched CGM at  $z = 2.2$  over the projected distance range from  $\approx 0.1 R_h$  to  $\approx R_h$ . The mean absorption strength of the metal-enriched CGM around starburst galaxies at  $z = 2.2$  is found to decline rapidly at beyond  $R_h$ . In addition, the observed mean absorber strengths at a fixed  $d/R_h$  remain to be stronger around these starburst galaxies than what is observed around either low-mass dwarf or high-mass galaxies at  $z \sim 0$ . The differential observed absorption strength versus  $R_h$ -normalized projected distance between low- and high-redshift galaxy samples suggests for the first time that the spatial absorption profile of the CGM may have evolved since  $z = 2.2$  (cf. Chen 2012). However, a direct comparison between the low- and high-redshift measurements is difficult because the high-redshift measurements were made in stacked spectra which presumably includes detections and non-detections among galaxies with a broad mass range (Table 3), and there was no distinction made between independent and group galaxies. An additional uncertainty also arises due to uncertainties in halo models (Diemer et al. 2013; see further discussions in § 5.3).

#### 4.4 Mean Absorption Profiles from Stacked CGM Spectra

To further improve upon the sensitivity in searching for weak absorption features and to facilitate a more direct comparison between our study and that of Steidel et al. (2010), we experiment with co-adding the absorption spectra of individual galaxies in the rest frame. We note, however, that interpreting the comparisons between low- and high-redshift measurements is not trivial (see § 5.3 for discussion).

For each input spectrum, we first mask contaminating features due to either the Milky Way interstellar medium or

<sup>5</sup> The inferred halo mass is a factor of two less than what is estimated by Steidel et al. (2010) or by Trainor & Steidel (2012) based on the observed galaxy clustering amplitude. For consistency, we adopt the halo mass estimate based on the stellar mass to halo mass relation.

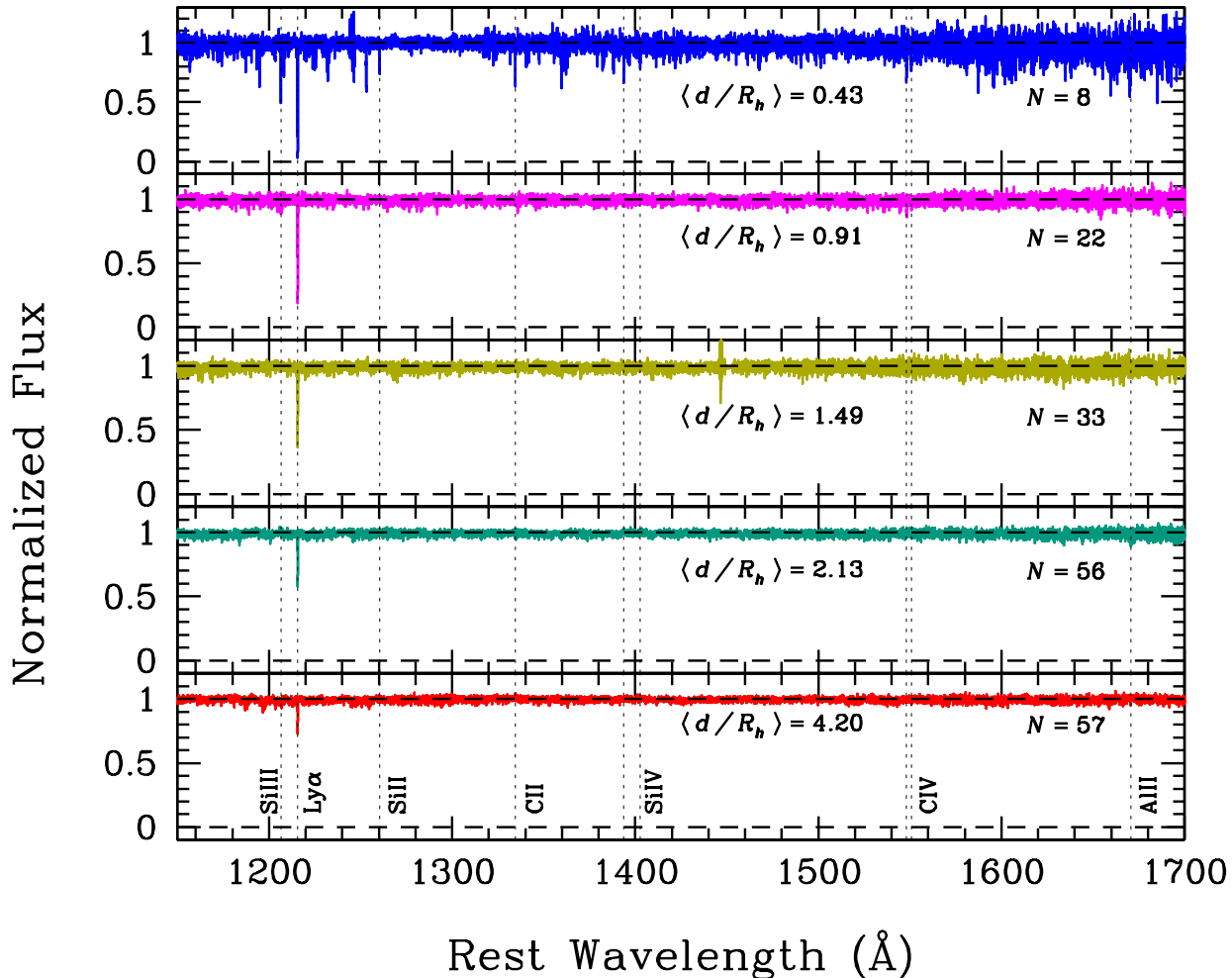


**Figure 9.** Stacked QSOs spectra in different  $R_h$ -normalized projected distance intervals from host galaxies. Galaxies at  $d < 1.7 R_h$  are grouped into three bins following the binning of the high-redshift starburst sample. Galaxies at  $d > 1.7 R_h$  are divided into two  $d/R_h$  bins with roughly equal number of galaxies. The median  $R_h$ -normalized projected distance and the number of galaxies included in each stack are indicated in each panel. The stacked spectra clearly show declining  $\text{Ly}\alpha$  absorption strengths with increasing projected distance, and no ionic transitions are detected with  $d/R_h > 0.7$ .

other strong absorbers at redshifts different from the foreground galaxy. Then each continuum normalized QSO spectrum and its associated error spectrum are shifted to the rest frame of the foreground galaxy. To account for the velocity offset between a galaxy and its associated absorbing gas (Figure 6), the rest frame of each galaxy is set to be the redshift of the observed  $\text{Ly}\alpha$  absorber<sup>6</sup>. For galaxies with no detected  $\text{Ly}\alpha$  absorbers, the rest frame is set to be the systemic redshift of the galaxy. Individual rest-frame spectra are then weighted and stacked to form a final mean spectrum. The weighting factor of each spectrum is defined as the inverse median variance which is determined using the associated error spectrum over the wavelength range from 1100 Å to 1450 Å in G130M data and from 1390 Å to 1750 Å in G160M data (e.g. columns 5 and 6 in Table 2).

We form different stacked CGM spectra for galaxies

grouped in different projected distance intervals, as well as in different  $R_h$ -normalized projected distance intervals. Given that a large fraction of detected heavy ions occur at  $d < 150$  kpc (left panels of Figures 7 & 8), we have adopted the first bin in projected distances to include galaxies at  $d < 150$  kpc and divided the remaining galaxies into three projected distance intervals with roughly equal number ( $N \approx 50$ ) of galaxies. For  $R_h$ -normalized measurements (right panels of Figures 7 & 8), we have adopted the same binning as the high-redshift starburst galaxy sample at  $d < 1.7 R_h$  and divided the rest of the galaxy sample into two  $d/R_h$  bins with roughly equal number ( $N \approx 56$ ) of galaxies. The stacked CGM spectra for different  $R_h$ -normalized distance intervals are presented in Figure 9.

In each stacked CGM spectrum, we measure mean absorption strengths of different transitions. However, uncertainty estimates of the observed mean absorption strengths in stacked spectra are complicated for two main reasons. First, Figures 7 and 8 show that in each  $d$  and  $d/R_h$  bin there is a combination of detections and non-detections. The mean

<sup>6</sup> We have also experimented with adopting the systemic redshift of the galaxies as the rest frame. No significant changes are seen.

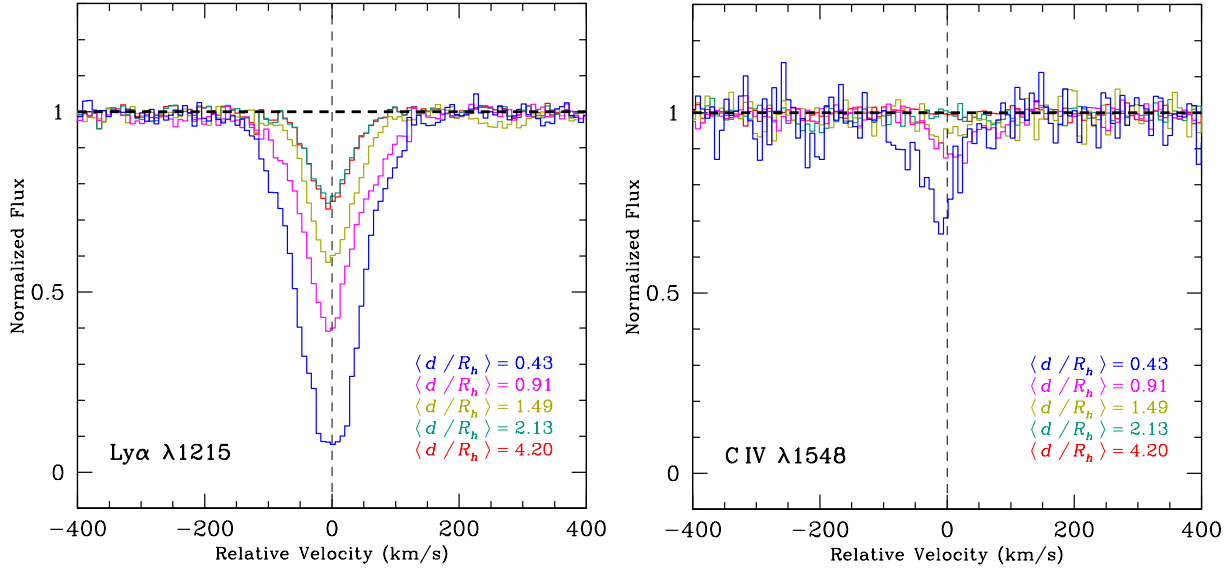


**Figure 10.** Mean absorption profiles of Ly $\alpha$  (left) and CIV (right) in stacked absorption spectra of galaxies in different  $d/R_h$  intervals.

properties of each stacked spectrum are therefore likely dominated by sampling errors. In addition, we have adopted an inverse-variance weighted mean to form each stacked spectrum. The final stacks may be dominated by one or two high  $S/N$  sightlines. To assess these sampling errors, we employ a bootstrap resampling technique.

For each subsample, we randomly sample the galaxies with replacement to construct a new subsample that contains the same number of input galaxies for stacking. We then measure the mean absorption equivalent width or a  $2\text{-}\sigma$  upper limit if no absorption features are found in the new stack. We repeat this exercise  $N_{\text{boot}}$  times and examine the distribution of the resulting mean absorption measurements. We find that a convergence is reached in the distribution when  $N_{\text{boot}} \gtrsim 350$ . We adopt the  $1\text{-}\sigma$  dispersion from the bootstrap resampling distribution as the uncertainties in the observed mean absorption in stacked spectra. In the case of non-detections, we quote the 95% upper bound of the distribution as the  $2\text{-}\sigma$  upper limit to the underlying absorption strength. The measurements and associated uncertainty estimates, as well as upper limits for non-detections are included in Figures 7 and 8 as solid blue points. The results are also summarized in Tables 5 and 6, which record for each distance interval the range of projected distance  $d$  (or  $d/R_h$ ), median projected distance  $\langle d \rangle$  (or  $\langle d/R_h \rangle$ ), the number of galaxies included in the stack, and the mean absorption strengths in Ly $\alpha$ , Si III, Si II, Si IV, C II, and CIV. Both Tables 5 & 6 and Figure 9 confirm that with higher  $S/N$  in the stacked spectra the mean Ly $\alpha$  absorption strength declines steadily with increasing projected distance, while no heavy ions are detected at 95% upper limits of  $W_0 \lesssim 0.03 \text{ \AA}$  at  $d \gtrsim R_h$ .

The strong upper limits presented in Tables 5 and 6 for non-detections demonstrate that using stacked spectra we are indeed able to improve the constraints for the presence/absence of absorbing gas by  $\sim \sqrt{N_{\text{gal}}}$ . No ionic transitions are found outside of galactic halos to unprecedentedly sensitive limits of better than  $0.03 \text{ \AA}$  at the  $2\text{-}\sigma$

level of significance. In addition, comparing the absorption-line measurements made in stacked CGM spectra confirms that massive starburst galaxies at  $z = 2.2$  (green symbols in the right panels of Figures 7 & 8) exhibit significantly stronger mean CGM absorption than the present-day galaxies (solid blue points). The differences are most pronounced in low-ionization species traced by C II and Si II absorption features. This is in stark contrast to the comparable mean absorption strengths of Mg II absorbers found at fixed luminosity-normalized projected distances (Chen 2012). The discrepancy is less for higher ionization species such as Si IV and CIV. Most interestingly, while we observe strong differential mean absorption strengths in different ionization states, such as between Si II and Si IV and between C II and CIV, the mean absorption strengths of different ions appear to be comparable at large distances from starburst galaxies at  $z = 2.2$ . The comparable strengths between low- and high-ionization transitions suggests that either the ionization condition in the high-redshift CGM is very different or the lines are saturated (in contrast to the non-saturated lines observed in our low-redshift sample) and therefore the line widths are driven by the underlying velocity field of the gas.

#### 4.5 Gas Covering Fraction

We have shown in § 4.4 that stacked CGM spectra enable strong limits on the possible presence of heavy elements outside of galactic halos, namely at projected distances  $d > R_h$ . Within galactic halos, however, the observed mean absorption strength in a finite distance interval is the product of the spatial absorption profile and partial gas covering. Figures 7 and 8 show that not only does the absorption equivalent widths of individual absorbers decrease with increasing distance, but the fraction of detections also decreases with increasing distance. An independent measure of the gas covering fraction is therefore necessary for an accurate characterization of the spatial absorption profile of the CGM.

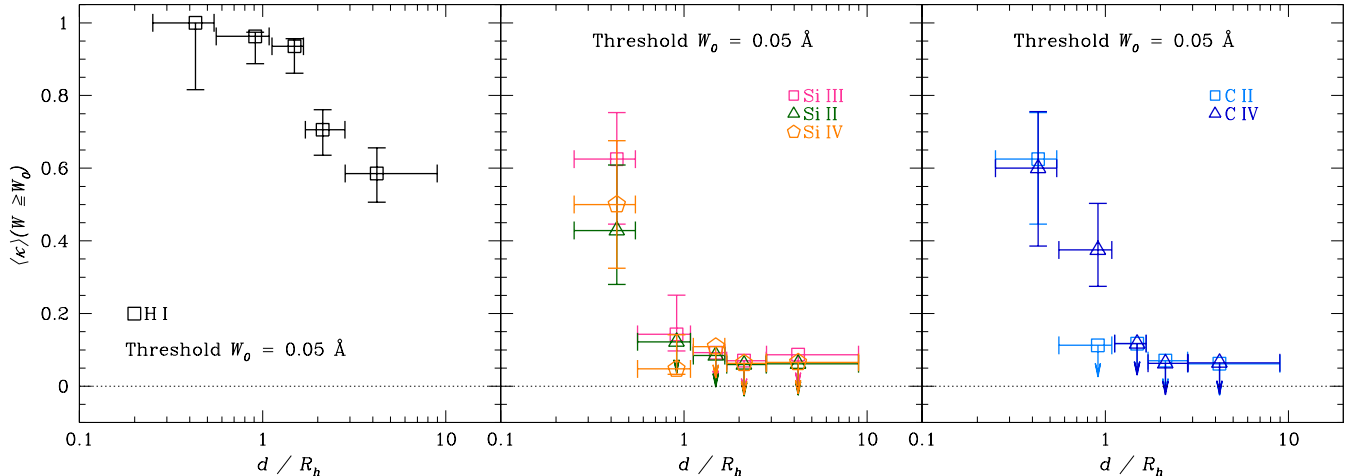


**Figure 11.** Mean gas covering fraction  $\langle \kappa \rangle$  measured in each  $d/R_h$  bin for different species. HI is shown in the left panel, Si II, Si III, and Si IV are shown in the middle panel, and C II and C IV are shown in the right panel. Gas covering fraction is computed for a detection threshold of  $W_0 = 0.05 \text{ \AA}$ . Error bars represent the 68% confidence interval. The covering fraction of Ly $\alpha$  absorbing gas remains high at  $\approx 60\%$  outside of dark matter halos at  $d > R_h$ , while the covering fraction of heavy ions is restricted to  $\langle \kappa \rangle < 10\%$  in individual  $d/R_h$  bins. Considering *all* galaxies at  $d > R_h$  further improves the limit on the covering fraction of heavy ions to  $\langle \kappa \rangle < 2\%$  at a 95% confidence level. In inner halos ( $d \lesssim 0.7 R_h$ ), we also find a declining mean covering fraction from high- to low-ionization species.

The large number of galaxies in our sample with sensitive limits available on the presence/absence of extended gas in individual galactic halos allows us to quantify how the covering fraction  $\kappa$  of absorbing gas varies as a function of projected distance based on an ensemble average. Here we consider galaxy subsamples defined in fixed  $d/R_h$  intervals in order to obtain a global average of how the gas covering fraction depends on halo radius-normalized distance.

Following the prescription described in Chen et al. (2010a), we employ a maximum likelihood analysis to estimate  $\kappa$  for different species. First, the probability that a galaxy inside a dark matter halo of radius  $R_h$  exhibits an absorber of rest-frame absorption equivalent width  $W_r \geq W_0$  at projected distance  $d$  is written as

$$P(\kappa|W_0) = \kappa(d/R_h) H[r_2 - d/R_h] H[d/R_h - r_1] \quad (4)$$

where  $H(x)$  is the Heaviside step function with  $H = 1$  if  $x > 0$  and  $H = 0$  otherwise, and  $r_1$  and  $r_2$  together define the distance interval over which  $\kappa$  is calculated. The likelihood function of observing an ensemble of  $n$  galaxies with associated absorbers of  $W_r \geq W_0$  and  $m$  galaxies with no absorbers detected to sensitive limits of  $W_r < W_0$  can then be written as

$$\begin{aligned} \mathcal{L}(\kappa|W_0) &= \prod_{i=1}^n \kappa(d_i/R_h^i) H[r_2 - d_i/R_h^i] H[d_i/R_h^i - r_1] \times \\ &\quad \prod_{i=1}^m (1 - \kappa(d_i/R_h^i) H[r_2 - d_i/R_h^i] H[d_i/R_h^i - r_1]) \\ &= \langle \kappa \rangle^n (1 - \langle \kappa \rangle)^m. \end{aligned}$$

Equation (5) is simply a binomial distribution function of a sample of  $m + n$  objects, in which  $n$  are detections,  $m$  are non-detections, and  $\langle \kappa \rangle$  represents the mean probability of detecting an absorber that maximizes the likelihood  $\mathcal{L}$ . In the form of a likelihood function, we are able to determine the confidence level for the best fit  $\langle \kappa \rangle$ . We evaluate  $\langle \kappa \rangle$  for  $W_0 = 0.05 \text{ \AA}$  by maximizing the likelihood function  $\mathcal{L}$  for different absorption transitions. Figures 7 and 8 show that the majority of the STIS and COS spectra included in our

analysis all have sufficient  $S/N$  to allow strong constraints for ruling out the presence of an absorber of  $W_r > 0.05 \text{ \AA}$  for all transitions considered in our study. In addition, at this sensitive limit of  $W_0 = 0.05 \text{ \AA}$ , we are already probing tenuous gas of HI column density  $\log N(\text{HI}) \lesssim 13$  or chemically enriched CGM of C IV column density  $\log N(\text{CIV}) \lesssim 13.5$ , assuming photo-ionized gas of  $T \sim 4 \times 10^4 \text{ K}$  (e.g. Bokenstein et al. 2003). Figure 11 shows the estimated  $\langle \kappa \rangle$  as a function of  $d/R_h$  for different transitions. Error bars in  $\langle \kappa \rangle$  represent the 68% confidence interval. For non-detections, we present the 95% single-sided upper limit. The results are also summarized in Table 7.

Figure 11 clearly shows that the covering fraction of Ly $\alpha$  remains high ( $\approx 60\%$ ) outside of dark matter halos at  $d > R_h$ , while the covering fraction of heavy ions is restricted to  $\lesssim 10\%$  in individual  $d/R_h$  bins. Considering *all* galaxies at  $d > R_h$  further improves the limit on the covering fraction of heavy ions to  $\langle \kappa \rangle_{\text{ions}} < 3\%$ . At  $d \approx 0.6 R_h$ , low-ionization transitions display a rapidly declining covering fraction from  $\langle \kappa \rangle \gtrsim 50\%$  at  $d = 0.2 - 0.6 R_h$  to  $\langle \kappa \rangle = 6\%$  and  $< 12\%$  at  $d = 0.6 - 1.1 R_h$  for C II and Si II, respectively. The high gas covering fraction at  $d \lesssim 0.6 R_h$  is consistent with measurements of  $\langle \kappa \rangle \approx 58 - 70\%$  for C II and Si II from the COS-Halos sample which probes inner galactic halos at  $d < 0.2 R_h$ , and with Mg II observations at  $d \lesssim 0.3 R_h$  by Chen et al. (2010a). In contrast, the covering fraction of (5) C IV declines from  $\langle \kappa \rangle = 60\%$  at  $d < 0.6 R_h$  to  $\langle \kappa \rangle = 38\%$  at  $d = 0.6 - 1.1 R_h$ . *Combining previous results with our findings suggests that halo gas becomes progressively more ionized from  $d \lesssim 0.2 R_h$  to larger distances.*

## 5 DISCUSSION

Based on absorption spectroscopy carried out in the vicinities of 195 galaxies at  $z \lesssim 0.17$ , we have obtained strong constraints for the absorption properties of the CGM at low

redshift. We observe distinct spatial absorption profiles between HI and heavy elements, with extended Ly $\alpha$  absorbing gas found at distances far beyond the halo radius  $R_h$  but no heavy ions detected at  $d \gtrsim 0.7 R_h$ . Here we discuss the implications of our study.

### 5.1 Observed Absence of Heavy Elements at $d \gtrsim 0.7 R_h$ from Star-forming Regions

A particularly interesting finding from our absorption-line search is that while between 60% and 90% of the galaxies at  $d \gtrsim 0.7 R_h$  show associated Ly $\alpha$  absorbers in the QSO spectra, all but two of these Ly $\alpha$  absorbers exhibit associated heavy ions to sensitive upper limits. The lack of detected heavy ions applies to both low-ionization species probed by the C II and Si II absorption transitions and high-ionization species probed by Si III, Si IV, and CIV. It implies that either the chemical enrichment in galactic halos has a finite edge at  $d \approx 0.7 R_h$  or gaseous clumps giving rise to the observed absorption lines cannot survive at these large distances.

In addition, the observed absence of heavy ions at  $d \gtrsim 0.7 R_h$  is found around galaxies that span over four orders of magnitudes in  $M_{\text{star}}$  (Figure 3). While the  $R_h$ -normalized radial profile in principle accounts for the size-scaling between galaxies of different mass, it does not include possible variations of halo gas properties as a result of the star formation history of the galaxies. Specifically, star formation rate is known to correlate strongly with galaxy mass (e.g. Figure 4) and star formation feedback is expected to substantially alter the physical properties of halo gas (e.g. Agertz & Kravtsov 2014). At the same time, high-mass galaxies of  $M_{\text{star}} \sim 10^{11} M_{\odot}$  are often found in quiescent mode with little on-going star formation (e.g. Muzzin et al. 2013), which would naturally result in a reduced absorption strength in halos around these massive galaxies (e.g. Gauthier et al. 2010).

To investigate possible variation in the  $R_h$ -normalized radial absorption profile of the CGM, we divide the galaxy sample into low- and high-mass subsamples. Figure 12 shows the CIV absorption properties for low-mass galaxies of  $M_{\text{star}} \lesssim 0.1 M_{\text{star}}^*$  (filled and open squares) and high-mass galaxies of  $M_{\text{star}} \gtrsim 0.1 M_{\text{star}}^*$  (filled and open circles), where  $M_{\text{star}}^* = 5 \times 10^{10} M_{\odot}$  (Baldry et al. 2012; Muzzin et al. 2013). Both low- and high-mass galaxies exhibit a modest mean covering fraction of strong ( $W_r(1548) > 0.1 \text{ \AA}$ ) CIV absorbers ( $\langle \kappa \rangle \approx 30 - 50\%$ ) at  $d < 0.7 R_h$ , and no associated CIV absorbers at  $d > R_h$ . The sample is too small to make a strong distinction, beyond  $R_h$ -normalization, in the extent of chemical enrichment between low- and high-mass halos in our sample.

A lack of heavy ions outside of the halos where dwarf galaxies reside provides important constraints for the amount of heavy elements that can escape these low-mass halos. Starburst driven outflows are thought to be particularly effective in removing baryons from low-mass halos because of a shallow potential well (e.g. Larson 1974; Martin 1999). Energetic outflows are also expected to suppress continuing growth of low-mass galaxies due to a reduced accretion rate (e.g. Scannapieco et al. 2001). These effects together can explain known scaling relations such as the mass-metallicity relation found in dwarf galaxies (e.g. Dekel

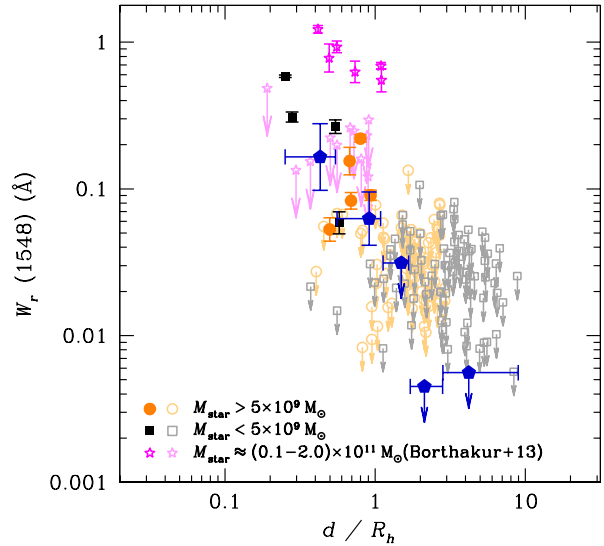


**Figure 12.**  $R_h$ -normalized radial profiles of CIV absorbing gas for low-mass galaxies of  $M_{\text{star}} < 0.1 M_{\text{star}}^*$  (filled and open squares) and high-mass galaxies of  $M_{\text{star}} > 0.1 M_{\text{star}}^*$  (filled and open circles), where  $M_{\text{star}}^* = 5 \times 10^{10} M_{\odot}$  (Baldry et al. 2012; Muzzin et al. 2013). Constraints from stacked spectra of the full sample are included for reference (pentagon points). Both low- and high-mass galaxies exhibit a modest mean covering fraction of strong ( $W_r(1548) > 0.1 \text{ \AA}$ ) CIV absorbing gas ( $\langle \kappa \rangle \approx 30 - 50\%$ ) at  $d < 0.7 R_h$ , and no associated CIV absorbers at  $d > R_h$ . No significant distinction, beyond  $R_h$ -normalization, can be made in the extent of chemical enrichment around low- and high-mass galaxies. In contrast, six of the 17 galaxies in the Borthakur et al. (2013) sample exhibit strong CIV absorption out to  $\sim R_h$  (star symbols). While the constraints for the 11 non-detections are weak, the detected CIV absorbers around six galaxies (four starburst and two passive galaxies) are all significantly stronger than the mean values observed in our sample.

& Woo 2003). However, model that predict enrichment levels to  $> 0.1$  solar metallicity are inconsistent with the observed limits we obtain at  $d > 0.7 R_h$  from low-mass dwarf galaxies at  $z \sim 0$ . This places an important constraint on feedback models that would enrich the CGM to much higher metallicity at these distances.

Our finding of a lack of detected heavy elements beyond  $d \approx 0.7 R_h$  appears to be discrepant from the observations of Borthakur et al. (2013), who reported detections of strong CIV out to  $d \sim R_h$  from massive galaxies of  $\log(M_{\text{star}}/M_{\odot}) \approx 10.1$  (star symbols in Figure 12). A possible explanation is to attribute the observed CIV absorbers to outflows driven by on-going star-formation activity, which indeed was part of the selection criterion of the Borthakur et al. sample. However, two of the galaxies with associated strong CIV absorbers are classified as quiescent galaxies with little on-going star formation since recent past.

An alternative scenario different from starburst driven outflows in explaining the presence of heavy elements at large distances is through gas stripping in an overdense group environment (e.g. Kawata & Mulchaey 2008; McCarthy et al. 2008). Such scenario can be tested with deep galaxy survey data of fields around these strong metal-line absorbers (e.g. Gauthier 2013).

To improve upon the detection limits of heavy ions in

Ly $\alpha$  absorbing gas, we repeat the stacking exercise discussed in § 4.4 but consider only galaxies at  $d \gtrsim R_h$  which exhibit associated Ly $\alpha$  absorbers. The goal of this exercise is to investigate whether some constraints can be obtained on the chemical enrichment level in known gaseous clouds revealed by Ly $\alpha$  absorption.

The absorption-line measurements and constraints in stacked spectra of Ly $\alpha$  absorbers are summarized in Table 8. We divide the galaxies at  $d \gtrsim R_h$  into three subsamples, each covering different  $R_h$ -normalized projected distance intervals. The goal is to maximize the  $S/N$  of the stacked spectra, while searching for possible trend of chemical enrichment with distance. In this particular exercise, we also search for the presence of the NV  $\lambda\lambda$  1238, 1242 doublet features. Similar to the OVI absorption doublet, the NV doublet is seen in highly ionized gas and is covered in the STIS and COS FUV spectral range. Observations of the NV absorption doublet together with CIV and other low-ionization transitions, therefore, provides a measure of the ionization state of the gas (see for example Figure 32 of Thom & Chen 2008). The results of our search remains the same; namely no ionic transitions are detected in Ly $\alpha$  absorbers at  $d \gtrsim R_h$  from galaxies in our sample. Adopting the absorption constraints for Ly $\alpha$  and CIV from Table 8 and assuming typical Doppler parameters,  $b(\text{HI}) = 30 \text{ km s}^{-1}$  (e.g. Tilton et al. 2012) and  $b(\text{CIV}) = 7 \text{ km s}^{-1}$  (e.g. Boksenberg et al. 2003), we infer a column density ratio of  $\log N(\text{CIV})/N(\text{HI}) < -1.3$ . In contrast, cosmological simulations that incorporate strong outflows to reproduce statistical properties of the general galaxy population in the low-redshift universe predict a column density ratio of  $\log N(\text{CIV})/N(\text{HI}) \sim -0.6$  at the virial radius of galactic halos of  $10^{11-12} M_\odot$  (Ford et al. 2013b). For photo-ionized gas, this column density ratio implies that the chemical enrichment level of Ly $\alpha$  absorbing gas at  $d \gtrsim R_h$  cannot exceed 0.1 solar metallicity.

## 5.2 The Origin of a Chemical Enrichment Edge at $\sim 0.7 R_h$

The distinct boundary between the presence and absence of metal-line absorbers at  $d \approx 0.7 R_h$  is seen in all ionic transitions that have been studied, including the observations of Si II, Si III, Si IV, C II, and C IV reported here and those of Mg II absorbers around  $\langle z \rangle = 0.24$  galaxies (Chen et al. 2010a). It is, however, not clear whether such absorption boundary exists for highly ionized gas probed by the OVI absorption doublet. Existing observations are primarily limited to inner galactic halos at  $d \lesssim 0.5 R_h$  (e.g. Tumlinson et al. 2011, 2013). Other studies that extend to larger radii have only small samples of “isolated” galaxies (e.g. Chen & Mulchaey 2009; Prochaska et al. 2011) and therefore available constraints are uncertain (see Johnson et al. 2014, in preparation).

A natural explanation for the chemical enrichment edge at  $d \approx 0.7 R_h$  is the turn-around radius  $r_{\text{turn}}$  of starburst driven outflows, similar to a halo fountain phenomenon (cf. Bregman 1980). We note that as chemically-enriched outflowing material moves into low-density regions and mixes in with metal-poor gas, it is expected that the outflowing material would be diluted and the observed absorption strength would gradually decline. However, to produce the

sharp downturn at  $d \approx 0.7 R_h$  would require a sharp decline in metallicity, which essentially indicates a finite edge of chemical enrichment and motivates the consideration of a turn-around radius of starburst driven outflows.

In this scenario, we can infer the launch speed as a function of launch radius of the outflows in individual halos. Adopting a Navarro-Frenk-White (NFW; Navarro et al. 1997) density profile for the underlying dark matter halos, we estimate the launch velocity  $v_{\text{out}}$  at a launch radius  $r_i$  following  $v_{\text{out}}(r_i) = \sqrt{2[\Phi(r_{\text{turn}}) - \Phi(r_i)]}$ , where  $\Phi$  is the gravitational potential and is related to radius  $r$  according to  $\Phi(r) = -(GM_s/r) \times \ln(1 + r/r_s)$ . For an NFW profile,  $r_s$  is the scale radius and  $M_s$  is the total mass enclosed within  $r_s$  and is related to the halo mass according to  $M_h = M_s [\ln(1 + R_h/r_s) - R_h/(r_s + R_h)]$ .

For galaxies in halos of  $M_h = 10^{11} M_\odot$ , which is typical of the mass range probed by our sample, we calculate a launch velocity of  $v_{\text{out}} \approx 170 \text{ km s}^{-1}$  at  $r_i = 1 \text{ kpc}$ . For lower-mass galaxies in halos of  $M_h = 10^{10} M_\odot$ , we find  $v_{\text{out}} \approx 75 \text{ km s}^{-1}$  at  $r_i = 1 \text{ kpc}$ . For higher-mass galaxies in halos of  $M_h = 10^{12} M_\odot$ , we find  $v_{\text{out}} \approx 330 \text{ km s}^{-1}$  at  $r_i = 1 \text{ kpc}$ . Naturally, a larger launch speed is required in more massive halos in order to reach out to a larger distance. Because more massive galaxies on average are forming stars at a higher rate (e.g. Salim et al. 2007), it is conceivable to have a higher outflow speed from starburst driven winds in a more massive galaxy. With a larger sample, we will be able to examine whether/how the metal-line boundary depends on star formation activity.

An alternative explanation for the observed finite metal-line boundary at  $d \approx 0.7 R_h$  is the critical radius below which cool clouds can develop and stabilize in a multi-phase medium (e.g. Maller & Bullock 2004; McCourt et al. 2012). Specifically, McCourt et al. (2012) showed that hot halos can develop extended multiphase structures if the cooling time  $t_{\text{cool}}$  is comparable to or less than the dynamical time  $t_{\text{ff}}$ . Given that  $t_{\text{cool}} \propto 1/\rho$  and  $t_{\text{ff}} \propto 1/\sqrt{\rho}$ , the ratio  $t_{\text{cool}}/t_{\text{ff}}$  decreases rapidly with decreasing radius. While the details depend on the exact density profile of the hot halo, it is conceivable that such condition can be reached at  $\approx 0.7 R_h$ .

Both the turn-around radius of starburst outflows and cooling radius of a hot halo can provide a physical explanation for the observed metal-line boundary. Because the former requires on-going star formation to provide the energy input, one can in principle distinguish between the two scenarios by examining whether or not the presence of a metal-line boundary depends on the star formation activity in the galaxies.

## 5.3 The CGM at Low and High Redshifts

When comparing a luminosity-normalized spatial extent of the CGM at different redshifts, Chen (2012) found that no distinctions can be made between low- and high-redshift galaxies that have dissimilar star formation histories. The adopted luminosity normalization was meant to account for a likely luminosity-size scaling relation commonly seen in optical disks (e.g. Cameron & Driver 2007). This approach was motivated by the expectation that the CGM is regulated by various complicated physical processes, including gravitational motion and star formation feedback. Normalizing the observed projected distance by the intrinsic lu-

minosity offers a means of accounting for the intrinsic size differences of individual galactic halos, and represents the first step toward establishing a clear understanding of the processes that drive the observed CGM properties. The results will facilitate future studies that consider the effect of additional processes such as star formation feedback.

But while rest-frame  $B$ -band luminosity ( $L_B$ ) is a good proxy of mass as shown in Chen et al. (2010b), it is an indirect measure of galaxy mass. Our study presented here utilizes a sample of galaxies with known stellar masses and normalizes the observed extent of halo gas by the inferred dark matter halo radius under a simple spherical overdensity approximation (e.g. Maller & Bullock 2004).

The finding in § 4.3 is surprisingly very different from the finding of Chen (2012). Specifically, when accounting for a size-scaling based on halo mass (instead of rest-frame  $B$ -band luminosity), high-redshift starburst galaxies exhibit both systematically stronger mean absorption strength at a fixed  $R_h$ -normalized projected distance at  $d/R_h \lesssim 0.7$  and more extended chemically-enriched gas to  $d \gtrsim R_h$  than low-redshift galaxies. Furthermore, the differences in the mean absorption strengths of the low- and high-redshift CGM are most pronounced in low-ionization species traced by C II and Si II absorption lines, suggesting distinct ionization conditions between the CGM at  $z \approx 0$  and at high redshifts near starburst galaxies.

We note, however, that a fundamental difference between the low- and high-redshift measurements is the treatment of galaxies with close neighbors. In our study presented here, we have considered only “isolated” galaxies with no known close neighbors spectroscopically identified within 500 kpc in projected distance and  $|\Delta v| < 500 \text{ km s}^{-1}$  in velocity separation. No such distinction was made in the high-redshift sample, and therefore the high-redshift CGM measurements include both isolated galaxies and those with neighbors. It has been suggested that galaxies in group environments display a more extended, chemically enrichment halo gas than galaxies in the field (e.g. Chen et al. 2010a; Bordoloi et al. 2011). At the same time, the overall cool gas content is also found suppressed in galaxy groups (e.g. Chynoweth et al. 2011). It is not clear that the more extended, strong CGM absorption around high-redshift starburst galaxies is due to a significant contribution of galaxies in group environments. A detailed study of the CGM in different group environments at low redshifts will be presented in a separate paper (Liang et al. 2014 in preparation).

In addition, Steidel et al. (2010) noted that the Si II absorption lines are saturated at  $d \lesssim 40$  kpc in the stacked low-resolution spectra. On the other hand, the ionic transitions observed in individual galaxies at low redshifts are not commonly saturated. Steidel et al. interpreted the observed declining absorption equivalent width (at least from  $d = 0$  to  $d = 40$  kpc) as likely due to a combination of decreasing line-of-sight velocity spread and decreasing covering fraction of the absorbing gas. In contrast, observations individual galaxies at low redshift indicate that the declining mean absorption equivalent width in stacked spectra is best explained by a declining gas covering fraction along with declining optical depth with increasing projected distance. Consequently, interpreting the observed difference between low- and high-redshift observations becomes more complicated.

At  $d > 40$  kpc, however, Steidel et al. (2010) also pointed out that the ionic absorption lines appeared to become unsaturated around high-redshift starburst galaxies. For unsaturated lines in stacked spectra, the observed declining equivalent width is best explained by a declining gas covering fraction along with a declining optical depth, similar to the low-redshift observations. Comparisons between our means stacked spectra and those from Steidel et al. could therefore be made for observations at  $d > 40$  kpc.

Remaining caveats include redshift uncertainties. Individual spectra of these high-redshift galaxies are of low  $S/N$  and low spectral resolution with FWHM  $\approx 350 \text{ km s}^{-1}$ . Random motions between galaxies and the absorbing gas (e.g. Figure 6) can smooth out the signal. Chen (2012) performed a simple Monte Carlo simulation to show that these uncertainties can result in an overall reduction of the absorption strength by  $\approx 20\%$ , increasing the discrepancy between low- and high-redshift samples. At the same time, uncertainties in sky subtraction of low  $S/N$  spectra may also bias the continuum estimate that is difficult to assess. It is expected that these uncertainties can be resolved with absorption spectroscopy of background QSOs near individual starburst galaxies (e.g. Rudie et al. 2012; Turner et al. 2014).

#### 5.4 Uncertainties due to Pseudo-evolution of Halo Radius $R_h$

We note, however, that a fundamental caveat in comparing  $R_h$ -normalized CGM profiles at different redshifts is in how  $R_h$  is calculated. Equations (2) and (3) outlines a commonly adopted approach to calculate halo mass  $M_h$  and halo radius  $R_h$  based on a spherical overdensity model. A dark matter halo is defined as a collapsed and virialized object with a mean enclosed density equal to  $\Delta_h$  times the mean background density  $\langle \rho_m \rangle$  at the redshift of interest. By this definition, however, as the universe expands,  $\langle \rho_m \rangle$  decreases. Consequently, both  $M_h$  and  $R_h$  would increase with time even for a static halo. Such pseudo-evolution of dark matter halos has been investigated by several groups, and a consistent finding in numerical simulations is that most halos of  $M_h \lesssim 10^{12} M_\odot$  completed matter accretion by  $z \sim 1$  with little/no net growth in mass over the last seven billion years (e.g. Prada et al. 2006; Diemand et al. 2007; Diemer et al. 2013). Therefore, applying an  $R_h$  normalization may impose a pseudo-evolution in the properties of galaxies residing in these low-mass halos.

Given the uncertainties in  $R_h$ , we explore different scaling relations for an accurate comparison of the CGM absorption profiles in different epochs. In Figure 13, we present CIV radial absorption profile normalized by the scaled radius  $r_s$  of the host dark matter halos (left panel) or by  $M_{\text{star}}$  of the absorbing galaxies (right panel).

The scale radius  $r_s$  represents a characteristic radius where the dark matter density profile resembles an  $r^{-2}$  profile (Navarro et al. 1997). The  $r_s$  normalization is motivated by the understanding that when a halo stops accreting, the scaled radius  $r_s$  remains constant while the halo mass  $M_h$  and halo radius  $R_h$  continue to increase as the universe expands and  $\langle \rho_m \rangle$  decreases. As a result, the halo concentration  $c \equiv R_h/r_s$  would also increase. Indeed, halo concentra-

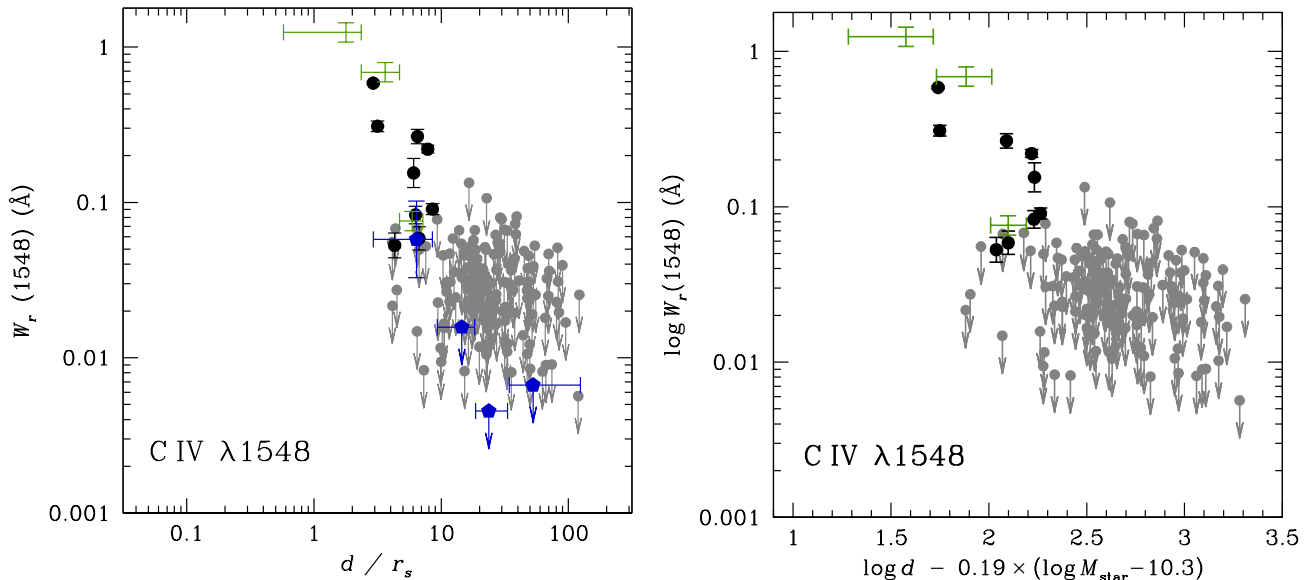


**Figure 13.** CIV radial absorption profile normalized by the scale radius  $r_s$  of the host dark matter halos (*left*) or by  $M_{\text{star}}$  of the absorbing galaxies (*right*). The scale radius  $r_s$  represents a characteristic radius where the dark matter density profile resembles an  $r^{-2}$  profile (Navarro et al. 1997). We also include in the left panel measurements from stacked spectra using the full galaxy sample (blue pentagons). In addition, the scaling coefficient of  $M_{\text{star}}$  is not a best fit to the CIV data, but adopted from the best-fit coefficient of Mg II absorbers from Chen et al. (2010b). Nonetheless, the result already reveals a clear CIV enriched halo out to  $M_{\text{star}}$ -normalized projected distance of  $\approx 160$  kpc (consistent with the finding of  $L_B$ -normalized CIV profile from Chen 2012). In both panels, the CIV radial absorption profiles at  $\langle z \rangle = 0.041$  (solid points) and at  $\langle z \rangle = 2.2$  (green crosses) appear to be better aligned than what is seen in the bottom right panel of Figure 7 & 8.

tions are found to increase rapidly for halos of  $M_h \lesssim 10^{12} M_\odot$  at  $z \lesssim 1$  (e.g. Zhao et al. 2009).

To calculate  $r_s$ , we adopt the mean  $c$ - $M_h$  relation of Zhao et al. (2009), which parameterizes  $c$  as a function of halo mass and redshift,  $c(M_h, z)$ . The left panel of Figure 13 shows that the  $r_s$ -normalized CIV radial profile at  $\langle z \rangle = 2.2$  declines rapidly at  $d \approx (4 - 6)r_s$ . This is consistent with observations of the  $\langle z \rangle = 0.041$  sample that display a covering fraction of CIV absorbing gas at  $d < 6r_s$  with  $\langle \kappa \rangle_{\text{CIV}} \approx 50\%$  and no detections found beyond  $8r_s$ .

The agreement in the  $r_s$ -normalized CGM absorption profiles at low and high redshifts is in stark contrast to the distinction seen in the  $R_h$ -normalized CGM profiles presented in Figures 7 & 8. We note, however, an inherent uncertainty in  $r_s$  as a result of the scatter in the mean  $c$ - $M_h$  relation ( $\sim 0.15$  dex). Nonetheless, it underscores the fundamental difficulty in making direct comparisons of galaxies and their halo gas properties in two different epochs.

A pseudo-evolution in dark matter halo mass (and therefore halo radius  $R_h$ ) has important implications beyond a constant CGM radial absorption profile. It would also suggest that chemical enrichment have reached out to the “edge” of the dark matter halo ( $\sim 4r_s$ ) or likely beyond, although a clear border for the observed metal-line absorbers outside of halo radius still implies a finite extent of chemical enrichment around galaxies. To quantify the extent of chemical enrichment, we will rely on numerical simulations as a guide for determining the physical size of the underlying dark matter halos of our galaxies. Such study is beyond the scope of this paper. We defer the analysis to a future paper (Liang et al. 2014, in preparation).

Given the uncertainty in  $R_h$  and  $r_s$  from dark matter

halo models, we return to applying empirical properties of the galaxies for scaling halo gas properties. Instead of  $B$ -band luminosity, however, we consider normalizing the projected distance of galaxies by stellar mass,  $M_{\text{star}}$ . The right panel of Figure 13 shows the  $M_{\text{star}}$ -normalized CIV radial profiles for the high- and low-redshift galaxy samples. We note that the adopted scaling coefficient of  $M_{\text{star}}$  is not a best fit to the CIV data, but adopted from the best-fit coefficient of Mg II absorbers from Chen et al. (2010b). Nonetheless, the result already reveals a clear CIV enriched halo out to  $M_{\text{star}}$ -normalized projected distance of  $\approx 160$  kpc (in an excellent agreement with the finding of  $L_B$ -normalized CIV profile from Chen 2012). Similar to the  $r_s$ -normalized profiles in the left panel, the  $M_{\text{star}}$ -normalized CIV radial absorption profiles at  $\langle z \rangle = 0.041$  and at  $\langle z \rangle = 2.2$  appear to be well aligned. With in mind the uncertainty in  $R_h$  and the agreement in  $M_{\text{star}}$ -normalized CGM radial profile, we therefore conclude that no strong evidence has been found to show a vastly different spatial distribution in the CGM absorption properties, despite a completely disparate star formation properties.

## 6 SUMMARY

We have analyzed archival UV spectra of QSOs located at projected distance  $d \leq 500$  kpc from 195 independent galaxies in the foreground. The redshifts of the galaxies range from  $z = 0.002$  to  $z = 0.176$  with a median of  $\langle z \rangle = 0.041$ , and the projected distances of the QSOs range from  $d \approx 32$  kpc to  $d \approx 500$  kpc with a median of  $\langle d \rangle = 362$  kpc. The galaxy sample covers a broad range in stellar mass from

$M_{\text{star}} = 1.5 \times 10^5 M_{\odot}$  to  $M_{\text{star}} = 1.4 \times 10^{11} M_{\odot}$ . The median and  $1\text{-}\sigma$  dispersion of stellar masses in the sample are  $\log(M_{\text{star}}/M_{\odot}) = 9.7 \pm 1.1$ . The available UV spectra of the QSOs allow us to study the multiphase CGM based on observations of a suite of absorption features including Ly $\alpha$ , C II, C IV, Si II, Si III, and Si IV. Using this large QSO and galaxy pair sample, we have obtained strong constraints for the absorption properties of the CGM at  $z \lesssim 0.176$ . The results of our analysis are summarized as the following:

(1) We observe a stark contrast between the spatial distributions of hydrogen atoms and heavy elements. While hydrogen gas is observed all the way out to 500 kpc in projected distance with a mean covering fraction of  $\approx 60\%$ , the same galaxies that display moderately strong H I absorption exhibit few associated metal absorption lines at  $d > 200$  kpc. The lack of heavy elements at large distances persists through all ionization states included in the study, suggesting that either there exists a chemical enrichment edge at  $d \approx 0.7 R_h$  or gaseous clumps giving rise to the observed absorption lines cannot survive at these large distances.

(2) The distinction between chemically-enriched and metal-poor gas is further enhanced after accounting for a mass scaling of gaseous radius in galactic halos. We infer a halo mass  $M_h$  and halo radius  $R_h$  for each galaxy based on the known stellar mass  $M_{\text{star}}$ , and find that no ionic transitions are detected at  $d \gtrsim 0.7 R_h$  to sensitive upper limits of rest-frame absorption equivalent width  $W_r \approx 0.05 \text{ \AA}$  or better. The observed absence of heavy elements at  $d \gtrsim 0.7 R_h$  applies to both low-mass dwarfs and high-mass galaxies. Considering all galaxies at  $d > R_h$ , we place a strict *upper limit* for the covering fraction of heavy elements of 3% (at a 95% confidence level) over the projected distance range from  $R_h$  to  $9 R_h$ .

(3) To further improve upon the sensitivity in searching for weak absorption features, we experiment with co-adding the absorption spectra of individual galaxies in the rest frame. Using stacked spectra we are indeed able to improve the constraints for the presence/absence of absorbing gas by factors of five to six. No ionic transitions are found at  $d > R_h$  to unprecedentedly sensitive limits of  $\approx 0.03 \text{ \AA}$  or better at the 95% confidence level.

(4) Within the gaseous halo probed by our galaxy-QSO pair sample, we observe differential covering fraction between low- and high-ionization gas. The mean covering fractions of both low- and high-ionization absorbing gas remain high at  $\langle \kappa \rangle \gtrsim 50\%$  over the distance range of  $d = (0.25 - 0.6) R_h$ . At  $d = (0.6 - 1) R_h$ , the covering fractions of C II and Si III decline to  $\langle \kappa \rangle \lesssim 14\%$ , while the covering fraction of C IV remains at  $\langle \kappa \rangle_{\text{C IV}} = 38\%$ . Combining previously observed high covering fraction of low-ionization gas in inner halos ( $d < 0.2 R_h$ ) with our findings suggests that halo gas becomes progressively more ionized from  $d < 0.2 R_h$  to larger distances.

(5) Combining our study of outer gaseous halos of low- and high-mass galaxies with the observations of the inner halos around massive galaxies from the COS-Halos program establishes a consistent  $R_h$ -normalized spatial absorption profile of the low-redshift CGM. Both the absorption strengths and incidence (covering fraction) of heavy elements decline steeply beyond  $0.3 R_h$  and become vanishingly small beyond  $0.7 R_h$ . In contrast, massive starburst galaxies at  $z = 2.2$  exhibit significantly stronger mean absorption than galaxies at

$z \sim 0$ . The differences are most pronounced in low-ionization species traced by C II and Si II absorption features, suggesting distinct ionization conditions between the CGM at low and high redshifts.

(6) We caution a potential pseudo-evolution in the CGM radial absorption profiles, when utilizing  $R_h$ -normalized projected distances to account for the intrinsic size difference between galaxies of different halo mass. The commonly adopted spherical overdensity calculation for halo mass imposes a pseudo-evolution for static halos as the universe expands and the mean matter density decreases with time. Normalizing the observed CGM radial profile by the scale radius  $r_s$  or by the stellar mass  $M_{\text{star}}$  confirms the previous finding that no significant changes can be found between the CGM at  $z \approx 2.2$  and  $z \approx 0$ .

## ACKNOWLEDGMENTS

This work has benefited from valuable discussions with Benedikt Diemer, Jean-René Gauthier, Nick Gnedin, Sean Johnson, and Andrey Kravtsov. We thank Andrey Kravtsov for providing the  $M_{\text{star}} - M_h$  relation during the preparation of this paper, Michael Blanton for referring us to the NASA-Sloan Atlas, and Alice Shapley and Naveen Reddy for providing a representative stellar mass distribution of the galaxy sample included in the study of Steidel et al. (2010). We also thank an anonymous referee for insightful comments that helped improve the presentation of the paper. This research has made use of the NASA/IPAC Extragalactic Database (NED) which is operated by the Jet Propulsion Laboratory, California Institute of Technology, under contract with the National Aeronautics and Space Administration. Some of the data presented in this paper were obtained from the Mikulski Archive for Space Telescopes (MAST). STScI is operated by the Association of Universities for Research in Astronomy, Inc., under NASA contract NAS5-26555. Support for MAST for non-HST data is provided by the NASA Office of Space Science via grant NNX13AC07G and by other grants and contracts.

**Table 1.** Summary of Galaxy Properties<sup>a</sup>

Galaxy Name	RA(J2000)	Dec(J2000)	$z_{\text{gal}}$	$\log \frac{\text{SFR}^b}{M_{\odot}/\text{yr}}$	$\log \frac{M_{\text{star}}}{M_{\odot}}$	$\log \frac{M_h^c}{M_{\odot}}$	$R_h$ (kpc)	$M_{\text{SDSS},r}^d$	Flag <sup>e</sup>
SDSS J000545.07+160853.3	00:05:45.07	+16:08:53.26	0.0372	-0.76	9.3	11.2	137.0	-18.8	0
SDSS J000548.11+161123.4	00:05:48.12	+16:11:23.40	0.1134	...	10.5	11.9	217.1	-21.2	1
2MASX J000556.17+160804.1	00:05:56.16	+16:08:04.17	0.0909	...	10.7	12.0	241.5	-21.5	1
SDSS J004208.22-102929.1	00:42:08.23	-10:29:29.10	0.0421	-0.50	9.3	11.2	133.6	-19.0	0
SDSS J004214.99-104414.9	00:42:14.99	-10:44:14.90	0.0360	-0.88	9.5	11.3	144.9	-19.6	0
SDSS J022617.97+001203.8	02:26:17.97	+00:12:03.85	0.0913	...	9.8	11.4	153.8	-19.7	1
2MASX J024248.74-082356.3	02:42:48.70	-08:23:56.65	0.0144	-1.83	9.7	11.3	154.7	-19.0	0
SDSS J025405.61-005236.6	02:54:05.64	-00:52:36.35	0.0032	-2.33	7.1	10.0	55.8	-13.9	0
SDSS J025906.86+004306.4	02:59:06.87	+00:43:06.34	0.0432	-1.19	8.9	11.0	118.2	-17.7	0
SDSS J025914.53+003359.6	02:59:14.53	+00:34:00.73	0.0092	-2.44	7.2	10.1	60.6	-15.5	0
SDSS J025938.43+003939.3	02:59:38.44	+00:39:39.24	0.0311	-1.53	8.0	10.5	83.0	-16.8	0
2MASX J025942.96+003907.8	02:59:42.94	+00:39:08.19	0.1342	...	11.0	12.4	327.2	-22.2	1

<sup>a</sup> The full table in machine-readable form is available at [http://lambda.uchicago.edu/public/local/galaxy\\_table.dat](http://lambda.uchicago.edu/public/local/galaxy_table.dat).

<sup>b</sup> Star formation rate derived from GALEX Near UV band with  $\lambda_{\text{eff}} \approx 2267 \text{ \AA}$ .

<sup>c</sup> The halo mass  $M_h$  and halo radius  $R_h$  are estimated following the prescription described in § 4.3.

<sup>d</sup> Absolute  $r$  band magnitude estimated from Seric + Exponential light profile fit (Bernadi et al. 2009).

<sup>e</sup> Galaxies with  $M_{\text{star}}$  from the NASA-Sloan Atlas are noted as “0”, and galaxies with  $M_{\text{star}}$  inferred from Equation (1) are noted as “1”.

**Table 2.** Summary of Observations of QSOs<sup>a</sup>

QSO Name	RA(J2000)	Dec(J2000)	$z_{\text{QSO}}$	PID	$S/N_{\text{G130M}}^b$	$S/N_{\text{G160M}}^b$	$S/N_{\text{STIS}}^c$
PG 0003+158	00:05:59.24	+16:09:49.01	0.4509	12038	16	13	...
SDSS J004222.29-103743.8	00:42:22.29	-10:37:43.79	0.4240	11598	6	4	...
SDSS J022614.46+001529.7	02:26:14.44	+00:15:30.04	0.6151	11598	8	5	...
SDSS J024250.85-075914.2	02:42:50.86	-07:59:14.25	0.3777	12248	6	5	...
SDSS J025937.46+003736.3	02:59:37.47	+00:37:36.38	0.5342	12248	6	5	...
PKS 0312-770	03:11:55.25	-76:51:50.85	0.2252	8651	...	...	5
SDSS J040148.98-054056.5	04:01:48.98	-05:40:56.58	0.5701	11598	6	5	...
PKS 0405-123	04:07:48.43	-12:11:36.66	0.5726	11541	...	...	48
RX J0439.6-5311	04:39:38.72	-53:11:31.40	0.2430	11520	11	7	...
HE 0439-5254	04:40:12.02	-52:48:17.70	1.0530	11520	11	8	...

<sup>a</sup> The full table in machine-readable form is available at [http://lambda.uchicago.edu/public/local/qso\\_table.dat](http://lambda.uchicago.edu/public/local/qso_table.dat).

<sup>b</sup> Median  $S/N$  of COS G130M grating in spectral range of 1150 – 1450Å and G160M grating in 1450 – 1750Å.

<sup>c</sup> Median  $S/N$  of STIS spectra in spectral range of 1200 – 1700Å.

**Table 3.** Available Absorption Constraints of Different Galaxy Samples

	# of Galaxies	$\langle z \rangle^a$	$d$ Range probed (kpc)	$\langle \log M_{\text{star}}/M_{\odot} \rangle^b$	Transitions <sup>c</sup>
This work	195	$0.04 \pm 0.04$	32 – 500	$9.7 \pm 1.1$	Ly $\alpha$ , C II, C IV, Si II, Si III, Si IV
Werk et al. 2013	44	$0.22 \pm 0.05$	18 – 154	$10.6 \pm 0.5$	Ly $\alpha$ , C II, Si II, Si III, Si IV
Steidel et al. 2010	512	$2.2 \pm 0.3$	10 – 125(280) <sup>d</sup>	$9.9 \pm 0.5^e$	Ly $\alpha$ , C II, C IV, Si II, Si IV

<sup>a</sup> Median redshift and dispersion of the galaxy samples.

<sup>b</sup> Median stellar mass and dispersion of the galaxy samples.

<sup>c</sup> Including only transitions common to this work.

<sup>d</sup> Maximum impact parameter is 280 kpc for Ly $\alpha$  and 125 kpc otherwise.

<sup>e</sup> Median and dispersion of stellar mass for Steidel et al. 2010, which is a representative sample of galaxies in Reddy et al. 2012.

**Table 4. Summary of Individual Halo Absorption Properties.**<sup>a, b</sup>

Galaxy	$\theta$ ( $''$ )	$d$ (kpc)	$z_{\text{gal}}$	$z_{\text{Ly}\alpha}$	HI $W_r(1215)$ (mÅ)	SiIII $W_r(1206)$ (mÅ)	SiII $W_r(1260)$ (mÅ)	SiIV $W_r(1393)$ (mÅ)	CII $W_r(1334)$ (mÅ)	CIV $W_r(1548)$ (mÅ)
SDSS J112644.33+590926.0	393.2	32.4	0.0040	0.0040	993 $\pm$ 15	290 $\pm$ 11	...	166 $\pm$ 12	106 $\pm$ 12	586 $\pm$ 12
SDSS J134249.99-005329.0	29.1	39.3	0.0708	0.0717	660 $\pm$ 16	78 $\pm$ 6	69 $\pm$ 8	$\leq$ 16	140 $\pm$ 14	309 $\pm$ 24
NGC 3485	582.5	57.6	0.0048	0.0048	506 $\pm$ 12	$\leq$ 22	$\leq$ 11	$\leq$ 21	$\leq$ 35	$\leq$ 22
SDSS J144520.23+341948.1	529	60.6	0.0056	0.0056	962 $\pm$ 94	$\leq$ 38	$\leq$ 20	$\leq$ 36	84 $\pm$ 19	266 $\pm$ 28
2MASX J08091327+4618424	68.6	62.7	0.0466	0.0464	1026 $\pm$ 10	54 $\pm$ 6	$\leq$ 11	69 $\pm$ 7	$\leq$ 21	$\leq$ 27
SDSS J122815.96+014944.1	1107.1	69.5	0.0030	0.0034	393 $\pm$ 8	$\leq$ 7	$\leq$ 4	$\leq$ 3	$\leq$ 5	$\leq$ 8
SDSS J121413.94+140330.4	56.6	70.1	0.0644	0.0644	859 $\pm$ 9	$\leq$ 6	$\leq$ 4	$\leq$ 10	$\leq$ 10	$\leq$ 15
2MASX J043936.88-530045.5	646.1	74.3	0.0056	0.0055	518 $\pm$ 9	152 $\pm$ 10	...	47 $\pm$ 8	$\leq$ 17	59 $\pm$ 10
SDSS J025914.53+003359.6	406	76.6	0.0092	0.0094	446 $\pm$ 33	...	$\leq$ 15	$\leq$ 29	$\leq$ 33	$\leq$ 39
SDSS J025938.43+003939.3	123.7	77.0	0.0311	0.0311	196 $\pm$ 12	$\leq$ 21	$\leq$ 28	$\leq$ 25	$\leq$ 31	$\leq$ 31

<sup>a</sup>The full table in machine-readable form is available at [http://lambda.uchicago.edu/public/local/absorber\\_table.dat](http://lambda.uchicago.edu/public/local/absorber_table.dat).<sup>b</sup>Upper limits are quoted at  $2\sigma$  level

**Table 5.** Absorption Equivalent Widths Observed in Stacked CGM Spectra in Different Projected Distance Range<sup>a</sup>

$d$ (kpc)	$\langle d \rangle^b$ (kpc)	Number	Ly $\alpha$ $\lambda$ 1215 (mÅ)	Si III $\lambda$ 1206 (mÅ)	Si II $\lambda$ 1260 (mÅ)	Si IV $\lambda$ 1393 (mÅ)	C II $\lambda$ 1334 (mÅ)	C IV $\lambda$ 1548 (mÅ)
32.4 – 138.1	86.1	17	486 ± 34	88 ± 13	45 ± 23	44 ± 16	48 ± 12	70 ± 37
156.2 – 307.1	243.2	52	295 ± 39	≤ 7	≤ 4	≤ 13	≤ 6	25 ± 12
311.0 – 442.4	383.9	54	136 ± 31	≤ 3	≤ 2	≤ 4	≤ 3	≤ 8
444.3 – 498.9	480.7	53	116 ± 23	≤ 4	≤ 6	≤ 6	≤ 5	≤ 6

<sup>a</sup> 1- $\sigma$  uncertainties and 2- $\sigma$  upper limits are determined from a bootstrap resampling calculation ( $N_{\text{boot}} = 350$ )

<sup>b</sup> Median impact parameter in each bin.

**Table 6.** Absorption Equivalent Width in Stacked CGM Spectra in different  $R_h$ -Normalized Projected Distance Range<sup>a</sup>

$d/R_h$	$\langle d/R_h \rangle^b$	Number	Ly $\alpha$ $\lambda$ 1215 (mÅ)	Si III $\lambda$ 1206 (mÅ)	Si II $\lambda$ 1260 (mÅ)	Si IV $\lambda$ 1393 (mÅ)	C II $\lambda$ 1334 (mÅ)	C IV $\lambda$ 1548 (mÅ)
0.25 – 0.54	0.43	8	550 ± 70	93 ± 32	67 ± 25	204 ± 94	102 ± 56	164 ± 86
0.56 – 1.09	0.91	22	382 ± 50	32 ± 15	≤ 4	≤ 34	≤ 6	63 ± 26
1.13 – 1.67	1.49	33	252 ± 31	≤ 4	≤ 5	≤ 20	≤ 8	≤ 31
1.71 – 2.82	2.13	56	165 ± 29	≤ 3	≤ 3	≤ 9	≤ 4	≤ 4
2.82 – 8.97	4.20	57	80 ± 14	≤ 10	≤ 3	≤ 3	≤ 4	≤ 6

<sup>a</sup> 1- $\sigma$  uncertainties and 2- $\sigma$  upper limits are determined from a bootstrap resampling calculation ( $N_{\text{boot}} = 350$ )

<sup>b</sup> Median  $R_h$ -normalized projected distance in each bin.

**Table 7.** Mean Gas Covering Fraction,  $\langle \kappa \rangle$ , of Different Species<sup>a</sup>

$d/R_h$	$\langle d/R_h \rangle^b$	Ly $\alpha$ $\lambda$ 1215	Si III $\lambda$ 1206	Si II $\lambda$ 1260	Si IV $\lambda$ 1393	C II $\lambda$ 1334	C IV $\lambda$ 1548
0.25 – 0.54	0.43	1.00 <sub>-0.18</sub>	0.63 <sup>+0.13</sup> <sub>-0.18</sub>	0.43 <sup>+0.18</sup> <sub>-0.15</sub>	0.50 <sup>+0.18</sup> <sub>-0.18</sub>	0.63 <sup>+0.13</sup> <sub>-0.18</sub>	0.60 <sup>+0.16</sup> <sub>-0.21</sub>
0.56 – 1.09	0.91	0.96 <sup>+0.01</sup> <sub>-0.08</sub>	0.14 <sup>+0.11</sup> <sub>-0.05</sub>	≤ 0.12	0.05 <sup>+0.09</sup> <sub>-0.02</sub>	0.06 <sup>+0.11</sup> <sub>-0.02</sub>	0.38 <sup>+0.13</sup> <sub>-0.10</sub>
1.13 – 1.67	1.49	0.94 <sup>+0.02</sup> <sub>-0.07</sub>	≤ 0.09	≤ 0.08	≤ 0.11	≤ 0.12	≤ 0.12
1.71 – 2.82	2.13	0.71 <sup>+0.05</sup> <sub>-0.07</sub>	≤ 0.07	≤ 0.06	≤ 0.06	≤ 0.07	≤ 0.06
2.82 – 8.97	4.20	0.59 <sup>+0.07</sup> <sub>-0.08</sub>	≤ 0.09	≤ 0.06	≤ 0.07	≤ 0.06	≤ 0.06

<sup>a</sup> Based on the fraction of absorbers with rest-frame absorption equivalent width greater than  $W_0 = 0.05$  Å.

<sup>b</sup> Median  $R_h$ -normalized projected distance in each bin.

**Table 8.** Absorption Equivalent Width in Stacked Spectra of Ly $\alpha$  Absorbers at  $d > 0.7 R_h$ <sup>a</sup>

$d/R_h$	$\langle d/R_h \rangle^b$	Number	Ly $\alpha$ 1215 (mÅ)	N V 1238 (mÅ)	Si III 1206 (mÅ)	Si II 1260 (mÅ)	Si IV 1393 (mÅ)	C II 1334 (mÅ)	C IV 1548 (mÅ)
0.96 – 1.63	1.26	32	308 ± 28	≤ 15	≤ 5	≤ 5	≤ 14	≤ 6	≤ 33
1.64 – 2.59	1.85	31	281 ± 34	≤ 8	≤ 6	≤ 8	≤ 15	≤ 15	≤ 17
2.59 – 8.97	4.06	30	131 ± 19	≤ 7	≤ 9	≤ 9	≤ 8	≤ 4	≤ 6

<sup>a</sup> 1- $\sigma$  uncertainties and 2- $\sigma$  upper limits are determined from a bootstrap resampling calculation ( $N_{\text{boot}} = 350$ )

<sup>b</sup> Median  $R_h$ -normalized projected distance in each bin.

## REFERENCES

- Adelberger, K. L., Shapley, A. E., Steidel, C. C., Pettini, M., Erb, D. K., & Reddy, N. A. 2005, *ApJ*, 629, 636
- Baldry, I. K.; Driver, S. P.; Loveday, J. et al. 2012 *MNRAS*, 421,621
- Barton, E. J. & Cooke, J. 2009, *ApJ*, 138, 1817
- Behroozi, P. S., Wechsler, R. H., Conroy, C., 2013, *ApJ*, 770, 36
- Blanton, M. R., & Roweis, S., 2007, *AJ*, 133, 734
- Blanton, M. R., Schlegel, D. J. Strauss, M. A. et al. 2005, *ApJ*, 129, 2562
- Blanton, M. R., Kazin, E. Muna, D., Weaver, B. A., Price-Whelan, A., 2011, *ApJ*, 142, 14
- Boksenberg, A., Sargent, W. L. W., Rauch, M., 2003, eprint arXiv:astro-ph/0307557
- Booth, C. M., Agertz, O., Kravtsov, A. V., Gnedin, N. Y., 2013, *ApJ*, 777, 5
- Bordoloi, R., Lilly, S. J., Knobel, C., et al. 2011, *ApJ*, 743, 10
- Bordoloi, R., Tumlinson, J., Werk, J. K. et al. 2014, *ApJ* submitted, arXiv:1406.0509
- Borthakur, S., Heckman, T., Strickland, D., Wild, V., Schiminovich, D., 2013, *ApJ*, 768, 20
- Bowen, D. V., Blades, J. C., Pettini, M., 1995, *AJ*, 448, 634
- Bregman, J. N. 1980, *ApJ*, 236, 577
- Cameron E., Driver S. P., 2007, *MNRAS*, 377, 523
- Chen, H.-W. & Tinker, J. L. 2008, *ApJ*, 687, 745
- Chen, H.-W. & Mulchaey, J. S. 2009, *ApJ*, 701, 1219
- Chen, H.-W., Lanzetta, Kenneth M.; Webb, John K.; Barcons, Xavier 1998, *ApJ*, 498, 77
- Chen, H.-W., Lanzetta, K. M., Webb, J. K., & Barcons, X. 2001a, *ApJ*, 559, 654
- Chen, H.-W., Lanzetta, K. M., & Webb, J. K. 2001b, *ApJ*, 556, 158
- Chen, H.-W., Helsby, J. E., Gauthier, J. R., Shectman, S.A., Thompson, I.B., Tinker, J.L., 2010a, *ApJ*, 714, 1521
- Chen, H.-W., Wild, V., Tinker, J. L., Gauthier, J.-R., Helsby, J. E., Shectman, S. A., Thompson, I. B., 2010b, *ApJ*, 724, L176
- Chynoweth, K. M., Holley-Bockelmann, K., Polisensky, E., & Langston, G. I. 2011, *ApJ*, 142, 137
- Colless, M., Dalton, G., Maddox, S. et al. 2001, *MNRAS*, 328, 1039
- Cooksey, K. L., Kao, M. M., Simcoe, R. A., O'Meara, J. M., Prochaska, J. X., 2013, *ApJ*, 763, 16
- Dekel, A. & Woo, J. 2003, *MNRAS*, 344, 1131
- Diemand, J., Kuhlen, M., & Madau, P. 2007, *ApJ*, 667, 859
- Diemer, B., More, S., & Kravtsov, A. V. 2013, *ApJ*, 766, 25
- Erb, D. K., Steidel, C. C., Shapley, A. E., Pettini, M., Reddy, N. A., & Adelberger, K. L. 2006, *ApJ*, 647, 128
- Ford, A. B., Oppenheimer, B., D., Davé, R., Katz, N., Kollmeier, J., A., & Weinberg, D. H. 2013a, *MNRAS*, 432, 89
- Ford, A. B., Davé, R., Oppenheimer, B. D., Katz, N., Kollmeier, J. A., Thompson, R., Weinberg, D. H., 2013b, eprint arXiv:1309.5951
- Fukugita M. & Peebles, P. J. E. 2004, *ApJ*, 616, 643
- Gauthier, J.-R. Chen, H.-W., Tinker, J. L., 2010, *ApJ*, 716, 1263
- Gauthier, J.-R., Chen, H.-W., 2011, *MNRAS*, 418, 2730
- Gauthier, J.-R., Chen, H.-W., 2012, *MNRAS*, 424, 1952
- Gauthier, J.-R., Chen, H.-W., Cooksey, K. L., Simcoe, R. A., Seyffert, E. N., O'Meara, J. M., 2013, eprint arXiv:1312.4593
- Gauthier, J.-R. 2013, *MNRAS*, 432, 1444
- Gehrels, N., 1986, *ApJ*, 303, 336
- Green, J. C., Froning, C. S., Osterman, S. et al. 2012, *ApJ*, 744, 15
- Haardt, F. & Madau, P., 2012, *ApJ*, 746, 125
- Huchra, J. P., Macri, L. M., Masters, K. L. et al. 2012, *ApJ*, 199, 22
- Hummels, C. B., Bryan, G. L., Smith, B. D., & Turk, M. J. 2013, *MNRAS*, 430, 1548
- Kacprzak, G. G., Churchill, C. W., Steidel, C. C., & Murphy, M. T. 2008, *AJ*, 135, 922
- Kawata, D., & Mulchaey, J. S., 2008, *ApJ*, 672, L103
- Kennicutt, R. C. Jr. & Evans, N. J. 2012, *ARA&A*, 50, 531
- Lanzetta, K. M., Bowen, D. V., Tytler, D., & Webb, J. K., 1995, *ApJ*, 442, 538
- Larson, R. B. 1974, *MNRAS*, 169, 229
- Maller, A. H. & Bullock, J. S., 2004, *MNRAS*, 355, 694
- Martin, C. L. 1999, *ApJ*, 513, 156
- McCarthy, I. G., Frenk, C. S., Font, A. S., Lacey, C. G.,

- Bower, R. G., Mitchell, N. L., Balogh, M. L., & Theuns, T., 2008, MNRAS, 383, 593
- McCourt, M., Sharma, P., Quataert, E., & Parrish, I. J. 2012, MNRAS, 419, 3319
- Mo, H. J., & Miralda-Escude J. 1996, ApJ, 469, 589
- Moustakas, J., Coil, A. L., Aird, J. et al. 2013, ApJ, 767, 34
- Murray, N., Menard, B., Thompson, T. A., 2011, ApJ, 735, 66
- Muzzin, A. Marchesini, D., Stefanon, M., et al. 2013, 777, 18
- Navarro, J. F., Frenk, C. S., & White, S. D. M. 1997, ApJ, 490, 493
- Oppenheimer, B. D. & Davé, R. 2008, MNRAS, 387, 577
- Prada, F., Klypin, A. A., Simonneau, E., Betancort-Rijo, J., Patiri, S., Gottlöber, S., & Sanchez-Conde, M. A. 2006, ApJ, 645, 1001
- Prochaska, J. X., Weiner, B., Chen, H.-W., Mulchaey, J. S., & Cooksey, K. L. 2011. 740, 91
- Rauch, M., Haehnelt, M. G., Steinmetz, M., 1997, ApJ, 481, 601
- Reddy, N. A., Pettini, M., Steidel, C. C., Shapley, A. E., Erb, D. K., & Law, D. R. 2012, ApJ, 754, 25
- Rudie, G. C., Steidel, C. C., Shapley, A. E., Pettini, M., 2013, ApJ, 769, 24
- Rudie, G. C., Steidel, C. C., Trainor, R. F., Rakic, O., Bogosavljevic, M., Pettini, M., Reddy, N., Shapley, A. E., Erb, D. K., & Law, D. R. 2012, ApJ, 750, 67
- Salim S. et al. 2007, ApJS, 173, 267
- Scannapieco, E., Thacker, R. J., & Davis, M. 2001, ApJ, 557, 605
- Schiminovich, D., Wyder, T. K., Martin, D. et al. 2007, ApJS
- Schiminovich, D., Catinella, B., Kauffmann, G., et al. 2010, MNRAS, 408, 919
- Shapley, A. E., Steidel, C. C., Erb, D. K., Reddy, N. A., Adelberger, K. L., Pettini, M., Barmby, P., Huang, J., 2005, ApJ, 626, 698
- Simcoe, R. A., 2011, ApJ, 738, 159
- Simcoe, R. A., Sargent, W. L. W., Rauch, M., 2004, ApJ, 606, 92
- Dreyer, J. L. E. 1988, "The Complete New General Catalogue and Index Catalogue of Nebulae and Star Clusters" ed. R. W. Sinnott (Sky Publishing Corporation and Cambridge University Press)
- Songaila, A., 2001, ApJ, 561, L153
- Spitzer L. 1956, ApJ 124, 20
- Steidel, C. C., Erb, D. K., Shapley, A. E., Pettini, M., Reddy, N. Bogosavljevic, M., Rudie, G. C., & Rakic, O. 2010, ApJ, 717, 289
- Stocke, J. T., Kenney, B. A., Danforth, C. W., et al. 2013, 763, 148
- Thom, C. & Chen, H.-W. 2008, ApJS, 179, 37
- Thom, C., Werk, J. K., Tumlinson, J., Prochaska, J. X., Meiring, J. D., Tripp, T. M., Sembach, K. R., 2011, ApJ, 736, 1
- Thom, C., Tumlinson, J., Werk, J. K., et al. 2012, ApJL, 758, L41
- Tilton, E. M., Danforth, C. W., Shull, J. M., & Ross, T. L. 2012, ApJ, 759, 112
- Trainor, R. F. & Steidel, C. C. 2012, ApJ, 752, 39
- Tripp, T. M., Lu, L., Savage, B. D., 1998, ApJ, 508, 200
- Tumlinson, J., Thom, C., Werk, J., 2013, ApJ, 777, 59
- Tumlinson, J., Thom, C., Werk, J. K. et al. 2011, Science, 334, 948
- Turner, M. L., Schaye, J., Steidel, C. C., Rudie, G. C., & Strom, A. L. 2014, MNRAS submitted (arXiv:1403.0942)
- Wakker, B. P. & Savage, B. D., ApJS, 182, 378
- Wang, B. 1993, ApJ, 415, 174.
- Werk, J., Prochaska, J., Thom, C., Tumlinson, J., Tripp, T. M., O'Meara, J. M., Peebles, & Molly S. 2013, ApJ, 204, 17
- Wild, V., Kauffmann, G., White, S., et al. 2008, MNRAS, 338, 227
- Woodgate, B. E., Kimble, R. A.; Bowers, C. W et al. 1998, PASP, 110, 1183
- York, D. G. Adelman, J.; Anderson, J. E., Jr. et al. 2000, ApJ, 120, 1579
- Zahid, H. J., Yates, R. M., Kewley, L. J., Kudritzki, R. P. 2013, ApJ, 763, 92
- Zhao, D. H., Jing, Y. P., Mo, H. J., & Börner, G. 2009, ApJ, 707, 354